TR-O-0062 40

# MMICデバイスプロセス技術

馬場　清一

1994.3.9

ATR光電波通信研究所

目次

# 復　帰　報　告　書

1994.02.28


氏名　　馬場　清一

所属　　ＡＴＲ光電波通信研究所
無線通信第２研究室　研究員


担当テーマ　　ＭＭＩＣデバイスプロセス技術

滞在期間　　平成２年３月１日～平成６年２月２８日


復帰先　　三洋電機（株）マイクロエレクトロニクス研究所
超高速デバイス基礎技術研究室
大阪府枚方市走谷 1-18-13
TEL : 0720-41-1276　FAX : 0720-41-7846


## 1　概要

ＡＴＲ光電波通信研究所では、腕時計型移動体通信器（リストフォン）の実現に向けて、モノリシックマイクロ波集積回路（ＭＭＩＣ）の超小型化・高集積化・高機能化の研究が進められてきた。その研究成果は [1]、線路一体化ＦＥＴおよび多層化ＭＭＩＣ技術として広く知られるようになり、本分野における業績は大きい。一方で、このような超小型移動端末器の存在を可能にする通信ネットワークとして、光ファイバミリ波サブキャリア伝送系の研究を進めてきた [2]。こうした新しい通信ネットワーク（情報処理も同様である）の概念を浸透させ、実現させるためには、必要とされる機能を集積回路化することが最も有効な手段であると考える。報告者は、超小型ＭＭＩＣの研究をさらに進展させ、またＭＭＩＣに光制御機能を付与する研究を行なった。ここでは、その研究成果の総括を目的とし、次の事項について述べる。

（１）多層化ＭＭＩＣ
（２）光マイクロ波集積回路（ＭＯＭＩＣ）・光集積回路

多層化ＭＭＩＣでは、薄膜線路、積層線路および結合線路の構成方法を提案し、また、これらを用いた各種マイクロ波回路の設計・試作を行なった。そして、高

性能・高機能な超小型ＭＭＩＣが実現できることを明かにした。一方、光マイクロ波集積回路では、マイクロ波素子としてのＨＥＭＴの光応答特性に着目し、その基本特性を明かにすると共に、光ファイバミリ波伝送系に適用した。そして、従来のｐｉｎ－ＰＤに比べて良好な伝送特性が得られ、集積化も容易であることを示した。また、報告者が提案した研究の幾つかはグループ内で進められ、大きく発展している。別途、テクニカルレポートを参考されたい。

### 参考文献


[1] 徳満「ＡＴＲにおける高周波回路の研究　－超小型・高機能ＭＭＩＣ－」ＡＴＲテクニカルレポート、ＴＲ－Ｏ－００２３、1990.03

[2] 小川「光ファイバを用いたミリ波サブキャリア伝送技術の研究」ＡＴＲテクニカルレポート、ＴＲ－Ｏ－００５５、1992.02


### 多層化ＭＭＩＣ

マイクロ波回路の構成方法として、多層化ＭＭＩＣには高いポテンシャルがある。本研究では、その特徴を活用した提案を行なうと共に、試作により実証することを目的とした。例えば、伝送線路の積層化によるハイブリッド回路の小型化及び、その能動回路への適用を図った。特に、増幅回路は線路一体化ＦＥＴ技術の適用外であり、多層化ＭＭＩＣの構成を用いて小型化した。さらに、マイクロ波回路の中で重要な役割を有する方向性結合器について、新しい構造を提案し、試作により小型で高性能な動作を確認した。本回路は、ミリ波／マイクロ波信号処理用ＭＭＩＣ（フィルタ、変調器、イコライザ等）にも適用でき、集積化できるマイクロ波回路の枠を広げるものである。以下に、超小型増幅器及び方向性結合器の構成と特性に関して述べる。

## 2　誘電体薄膜を用いた多層化ＭＭＩＣ増幅器

Miniaturized MMIC amplifiers utilizing a multilayer structure composed of thin film transmission lines are presented. The fundamental characteristics of the thin film transmission lines for use in microwave active circuits are discussed through calculations by numerical analysis. A two-stage low-noise amplifier, a single-stage wideband amplifier and a balanced amplifier are designed within very small areas, while good performance is maintained.

The results include that a Ka-band single-stage amplifier is fabricated in a 0.8 mm × 0.6 mm area with a gain of 8.0-9.5 dB in the frequency range of from 16.0 GHz to 26.5 GHz and input/output return losses of better than 8 dB at 26.5 GHz. The proposed amplifier configurations can be applied to high density integration of one-chip MMIC modules.

## 2.1 はじめに

Monolithic microwave integrated circuits (MMIC's), which will be essential components in future communication systems, must be miniaturized. Large-scale, complicated MMIC's are also required [1]. Fortunately, a thin film transmission line structure, which utilizes narrow-width microstrip conductors on thin (several-$\mu$m thick) dielectric materials fabricated over a ground plane metal on a GaAs wafer surface, was recently reported [2]-[6]. Thin film transmission lines allow for high density circuit integration due to reduced transmission line widths and their ready application to multilayer configurations. For example, thin film transmission lines such as microstrip, inverted microstrip and triplate lines can be applied to a multilayered transmission line structure using a ground plane metal, which serves to separate the transmission lines [7]. In addition, meander-like and cross-over transmission line structures are easily fabricated in a small area. Therefore, a highly flexible circuit design is achieved for a 3-dimensional structure, and this configuration can be used for high density integration of MMIC's. Thin film transmission lines can also be integrated within uniplanar microwave circuits [8]. Monolithic microwave integrated circuits using thin film transmission lines are usually called multilayer MMIC's. Several microwave passive circuits using thin film transmission

lines have been reported [2]-[4],[7].

However, design methods and applications for active circuits such as amplifiers and mixers have not been sufficiently discussed. Although thin film transmission lines can substantially reduce the circuit area, they show relatively high insertion losses compared with conventional microwave transmission lines such as microstrip and coplanar waveguide lines, and degrade circuit performance [4]. It is therefore important to optimize the structure of the transmission lines in the MMIC design.

In this paper, the fundamental characteristics of thin film transmission lines are calculated by the qusai-static and full-wave finite-element-method (FEM), and their suitability for use in microwave active circuits is demonstrated. A design method that allows reducing the chip area and obtaining good performance, is presented using numerical results and an equation. Thin film transmission line structures, that is, microstrip line-, inverted microstrip line- and triplate line-structures using polyimide films as the thin dielectric substrates are successfully utilized to realize miniaturized MMIC amplifiers. An X-band two-stage low-noise amplifier, a Ka-band single-stage wideband amplifier and a balanced amplifier are fabricated utilizing these transmission line structures, and their performance is also demonstrated. The intrinsic chip area of the amplifiers is about one-fourth that of conventional MMIC's.

## 2.2 薄膜伝送線路

The fundamental characteristics of microstrip, inverted microstrip and triplate lines using thin dielectric layers are discussed in this chapter. A schematic cross sectional view of these transmission lines is shown in Fig. 1.

Each transmission line is formed on a GaAs wafer surface. These structures consist of polyimide films for the thin dielectric layers and 1 $\mu$m-thick gold films for the conductor metals.

A process for polyimide film preparation and subsequent chemical etching is reported in [9]. This process can generate cone-shaped via-holes, which connect the microstrip conductors on the upper dielectric layers with the input/output ports and microstrip conductors on the lower dielectric layers. The relative dielectric constant and loss tangent of the polyimide film are 3.7 and 0.01 (10 MHz), respectively. A uniformity in the film thickness of better than 1% is obtained up to 10 $\mu$m. The measured stress of the polyimide film is a constant value of $-2.4 \times 10^8$ dyn/cm$^2$, and is one-tenth that of $Si_3N_4$ and $SiO_2$ films. Furthermore, the surface of the films, which is formed by spin-coating, is flat due to its high viscosity. These properties show polyimide film to be a suitable dielectric material for thin film transmission line fabrication. In our fabrication, the multilayer structure consists of two 5.0 $\mu$m-thick polyimide films to construct a three-layer conductor.

The calculated characteristic impedance and normalized guided wavelength ($\lambda_g/\lambda_o$) of these transmission lines are shown in Fig. 2. Because these structures are small in comparison with their guided wavelength, quasi-TEM approximation can be used for numerical analysis. For the inverted microstrip line and triplate line, the polyimide film flatness over the strip conductor, $\delta(N)$, must be considered, because the film thickness is somewhat decreased due to the presence of the lower conductor. The polyimide film flatness is

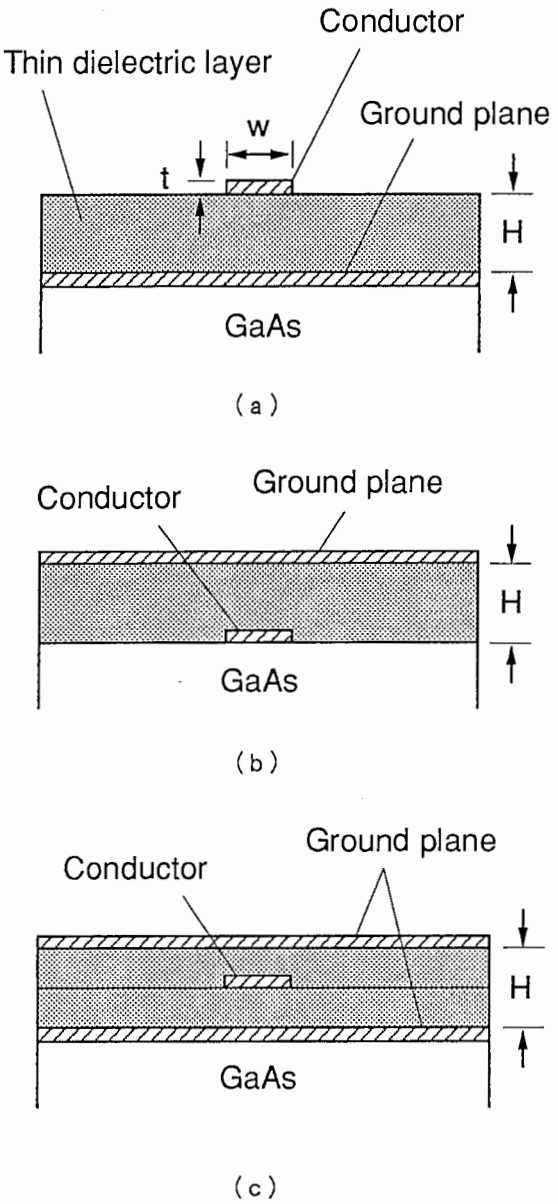


**Fig. 1** Basic transmission line structures using thin dielectric layers. (a) A microstrip line structure, (b) an inverted microstrip line structure and (c) a triplate line structure.

given by following equation.

$$\delta(N) = \left\{1 - \left(\frac{A}{B}\right)^N\right\} \times 100 \quad [\%], \tag{1}$$

where A, B and N are the ramp height after polyimide formation, initial conductor thickness and number of layer piles, respectively. According to our polyimide preparation conditions, the flatness of the first and second polyimide layers is 36% and 60%, respectively. The conductor widths of these transmission lines, whose characteristic impedances range from approximately 100 Ω to 15 Ω, are between 5 $\mu$m and 30 $\mu$m, and are similar to the polyimide film thickness. Furthermore, the conductor widths of these transmission lines are less than one-fifth those of the microstrip lines in conventional MMIC's. Therefore, a highly flexible circuit design can be achieved. The conductor widths of the microstrip, inverted microstrip and triplate lines, whose characteristic impedance is approximately 50 Ω, are 21 $\mu$m, 8 $\mu$m and 5 $\mu$m, respectively, when the total polyimide film thickness is 10 $\mu$m. Since the inverted microstrip line has a highly effective dielectric constant due to the GaAs substrate, the conductor width is 40% less than that of a microstrip line. The triplate line has a low characteristic impedance with a narrow conductor width. This result shows the triplate line to be a suitable structure for a low impedance line in amplifier circuits, compared with the other two. For example, the conductor width of a 20 Ω triplate line (H = 10 $\mu$m) is only approximately 20 $\mu$m.

## 2.3 薄膜伝送線路の損失

Thin film transmission lines show relatively high insertion losses, dominated by conductor losses, due to narrow widths of the microstrip conductors.

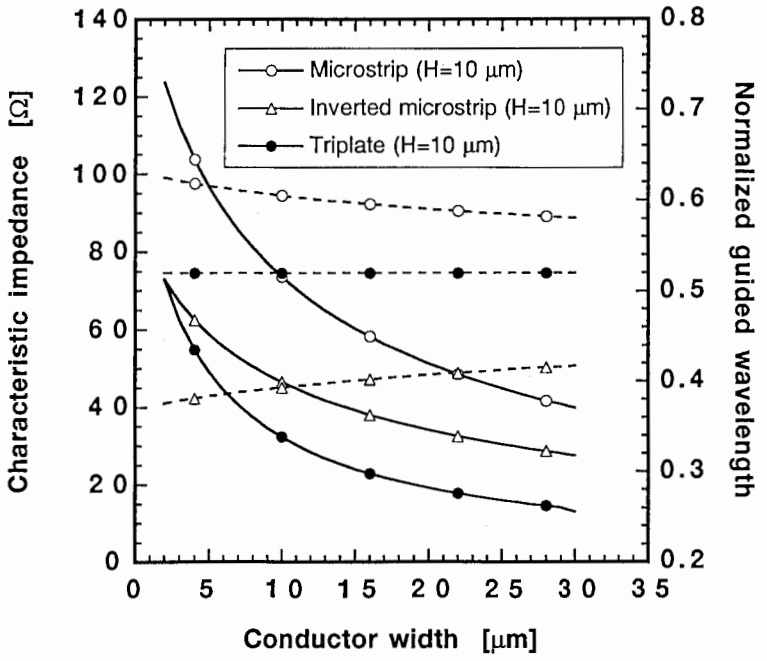


**Fig. 2** Calculated characteristic impedance (solid line) and normalized guided wavelength (dashed line : $\lambda_g/\lambda_o$) of various transmission lines as a function of the conductor width.

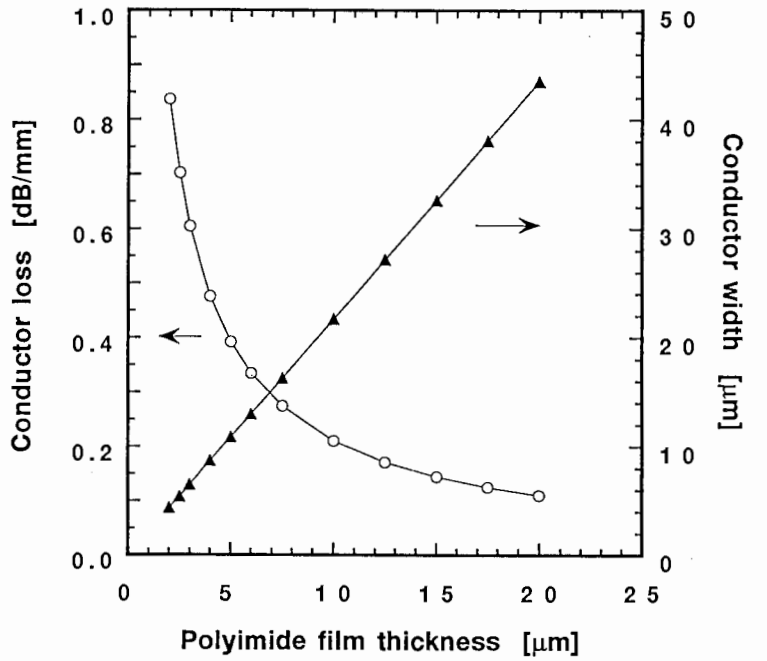


**Fig. 3** Calculated conductor loss and conductor width of 50 Ω microstrip lines as a function of the polyimide film thickness at a frequency of 20 GHz.

The conductor losses (at 20 GHz) of these transmission lines are calculated by full-wave FEM [10]. In the calculation, the skin effect is considered, because the conductor thickness is approximately two times greater than the skin depth of the conductor at 20 GHz. We also assume the surface roughness of the conductor to be zero, from observations by scanning electron microscopy (SEM). The calculated conductor losses of 50 $\Omega$ microstrip line structures as a function of the polyimide film thickness are shown in Fig. 3. The calculated results show that the conductor losses of the transmission lines decrease rapidly with increasing polyimide film thickness, and range from 0.84 dB/mm to 0.11 dB/mm for thicknesses of 2 $\mu$m to 20 $\mu$m; they show smaller improvements above 10 $\mu$m. The conductor losses of these transmission lines as a function of the conductor width, assuming polyimide thicknesses of 10 $\mu$m and 5 $\mu$m, are shown in Fig. 4. The calculated current distribution for the symmetrical half space of a microstrip line is shown in Fig. 5. The current concentrates near both edges of the microstrip conductor, and rapidly decreases for distances from the conductor edge up to 2.5 $\mu$m ($x/H = 0.25$). Therefore, the conductor losses of these transmission lines are slightly reduced for conductor widths of above 5 $\mu$m ($= H/2$). To reduce the transmission line loss, the thickness of the polyimide film and conductor width must be greater than 5 $\mu$m. Transmission lines having identical conductor widths and polyimide thicknesses show almost the same insertion losses (*per* $\lambda_g$) for different characteristc impedances. For example, a 50 $\Omega$ microstrip line and a 35 $\Omega$ inverted microstrip line with the same conductor width (W = 10 $\mu$m) have almost the same insertion loss (*per* $\lambda_g$), when the polyimide film thickness is 5 $\mu$m, as shown in Fig. 4.

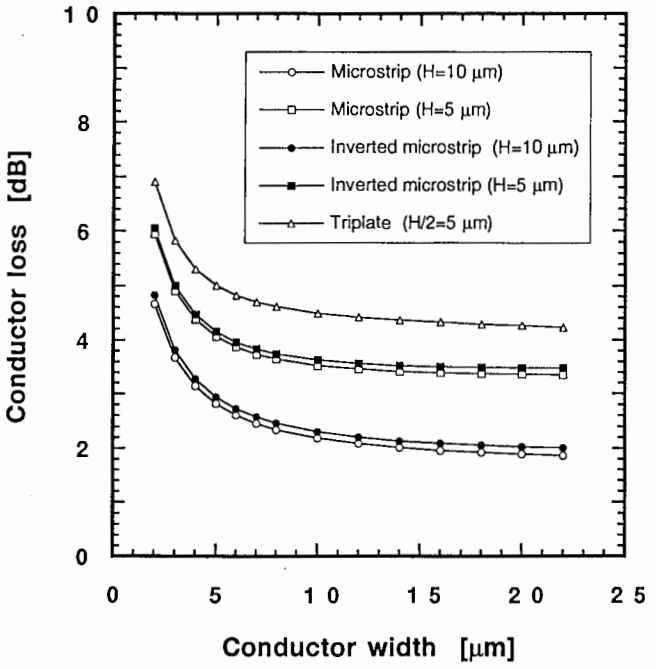


**Fig. 4** Calculated conductor loss (*per* $\lambda_g$) of various transmission lines as a function of the conductor width at a frequency of 20 GHz.

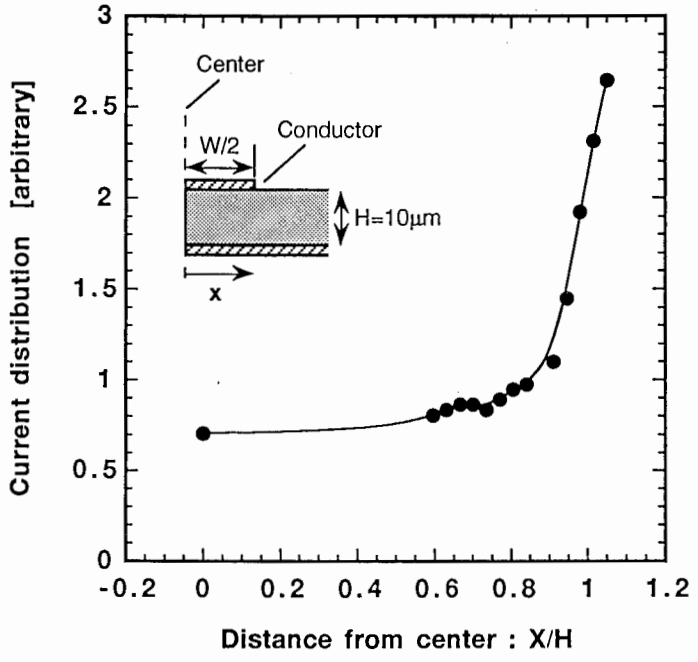


**Fig. 5** The current distribution for the symmetrical half space of a microstrip line ($H = 10\ \mu m$, $W = 21\ \mu m$, $W/H = 2.1$).

Losses in the microstrip line have been discussed in [2], [11], [12]. To calculate the circuit performance, we must simulate the frequency characteristic of the transmission line attenuation with a commercialy available CAD software package. The surface resistivity $R_s$ which is considered as the skin effect is given by (2),

$$R_s(f) = R_{so}tK \cdot \sqrt{f}/(1 - e^{-tK\sqrt{f}}) \qquad [\Omega/\square], \tag{2}$$

where $t$ and $K$ are the conductor thickness and material constant ($=\sqrt{\pi\sigma\mu}$), respectively. The conductor loss $\alpha_c$ is proportional to $R_s$,

$$\alpha_c(f)/\alpha_c(F) = R_s(f)/R_s(F). \tag{3}$$

The dielectric loss $\alpha_d(f)$ is estimated by using the following assumptions [13]: (i) The loss tangent of the polyimide film is proportional to the operating frequency, and (ii) the value of the loss tangent is 0.020 at 20 GHz.

$$\tan\delta(f)/\tan\delta(F) = f/F \tag{4}$$

$$\alpha_d(f) = \frac{27.3}{\lambda_g}\tan\delta(f) = 27.3 \cdot \frac{f}{c} \cdot \sqrt{\varepsilon_{eff}} \cdot \tan\delta(f) \qquad [dB/mm]. \tag{5}$$

Therefore, in the circuit design, the frequency characteristic of the total attenuation per unit length $\alpha(f)$ is given by the following equation, rewritting the calculated or evaluated value, $\alpha_c(F)$ or $\alpha_d(F)$, at a design frequency of $F$ (in our case $F = 20$ GHz).

$$\alpha(f) = \alpha_c(F) \cdot \sqrt{\frac{f}{F}} \cdot \frac{1 - e^{-tK\sqrt{F}}}{1 - e^{-tK\sqrt{f}}} + \alpha_d(F) \cdot \frac{f^2}{F^2} \qquad [dB/mm]. \tag{6}$$

The transmission lines are tested using on-wafer probes and an HP8510 network analyzer. The length of the measured transmission lines with coplanar waveguide (CPW) ports is 1.3 mm (intrinsic line length: 1.0 mm). Each

transmission line is connected to the CPW-ports through via-holes (15 $\mu$m $\times$ 15 $\mu$m) on a GaAs wafer surface, and the transition loss between every CPW-port and transmission line is less than 0.075 dB at 20 GHz. Fig. 6 shows the calculated and measured characteristics of a microstrip line. A good agreement between these values is obtained in the frequency range of 0-40 GHz using (6).

### 2.4 増幅器の設計と特性

An AlGaAs/InGaAs pseudomorphic HEMT with a T-shaped 0.25 $\mu$m-gate is applied to the amplifier circuits. The gate width and gate finger number of the HEMT are 100 $\mu$m and 2, respectively. The HEMT has a calculated cutoff frequency of 45 GHz, and its small-signal equivalent circuit is determined from S-parameter measurements up to 40 GHz as shown in Fig. 7. The noise parameters are characterized by using an on-wafer noise measurement system up to 18 GHz. The values of the noise figure, $\Gamma_{opt}$ and Rn are 1.05 dB, 0.571 $\angle$ 43.2° and 19.1 $\Omega$, respectively, at 12 GHz.

In the circuit design, we adopted a commercially available CAD software package, which includes a user defined function routine (Touchstone), to optimize circuit parameters by using (6) for the frequency characteristics of the transmission lines. Each transmission line has a meander-like configuration, and short-stub lines are arranged over the MIM (metal-insulator-metal) bypass capacitors to reduce the circuit area; each line is connected to the upper metal of the capacitors through the via-holes. Table 1 summarizes the structural parameters and calculated performance of the transmission lines in the fabricated amplifiers. For reference, values from conventional CPW structures are

**Table 1** Structural parameters and characteristics of thin film transmission lines for use in amplifiers. The losses are calculated at 20 GHz.

| | Structure | Line width [μm] | Polyimide thickness [μm] | Characteristic impedance [Ω] | Effective dielectric constant | Conductor loss [dB/mm] |
|---|---|---|---|---|---|---|
| (a) | Microstrip line | 10 | 10 | 75.0 | 2.73 | 0.241 |
| (b) | Microstrip line | 10 | 5 | 50.0 | 2.87 | 0.398 |
| (c) | Inverted microstrip line | 10 | 5 | 35.0 | 6.04 | 0.590 |
| (d) | Triplate line | 14 | 10 | 25.0 | 3.70 | 0.559 |
| (e) | Input / output CPW-port | Width / Gap = 42 / 29 | --- | 50.0 | 6.83 | 0.093 |
| (f) | CPW | Width / Gap = 12 / 10 | --- | 50.0 | 6.54 | 0.278 |

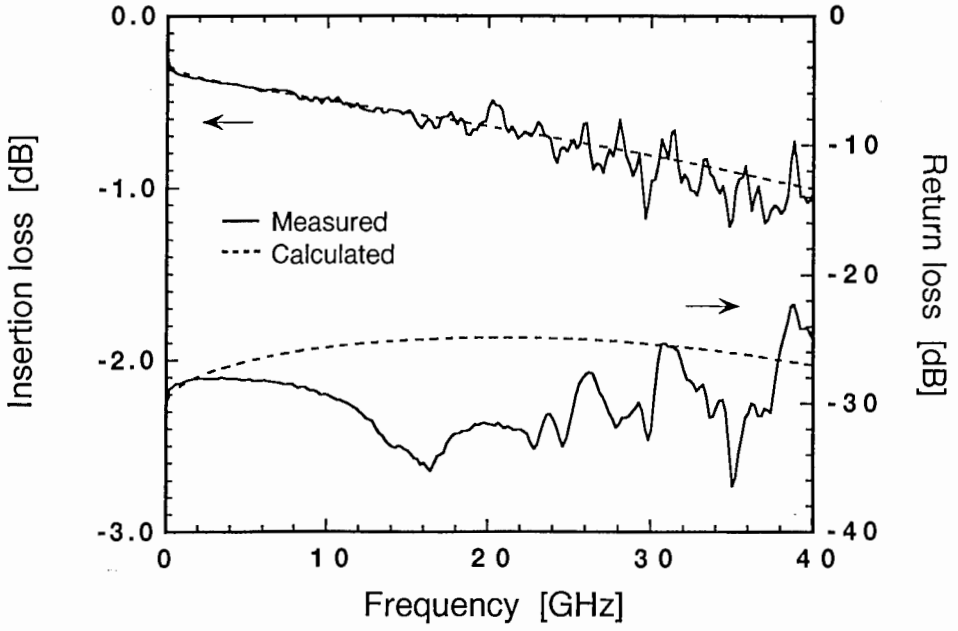


**Fig. 6** Calculated and measured frequency characteristics of a 50 Ω microstrip line. Solid line: measured, dashed line: calculated.

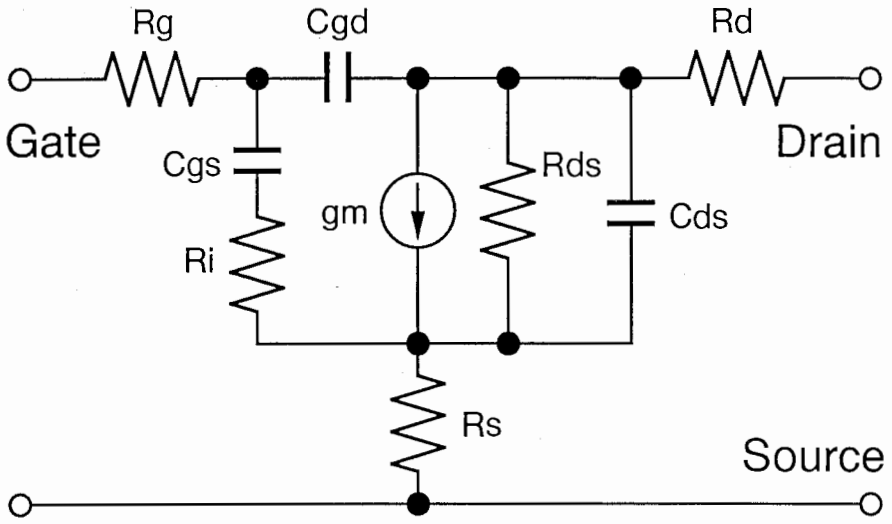


| | |
|---|---|
| gm = 49.4 mS | Rds = 407 Ω |
| Cgs = 110.6 fF | Rs + Ri + Rg = 3.76 Ω |
| Cgd = 34.3 fF | Rd = 3.85 Ω |
| Cds = 22.5 fF | taw = 1.32 psec |
| Lg = Ld = 0.021 nH | |

**Fig. 7** Small-signal equivalent circuit of a HEMT with a 100 $\mu$m width and 2-finger gate ($Vds = 3\ V$, $Idss = 20\ mA$).

also shown. The conductor widths of these transmission lines are less than 14 $\mu$m, and the gap of the strip conductors is about four times the conductor width and the dielectric thickness; therefore, the coupling effect of the transmission lines is almost eliminated.

### 2.4.1 X帯低雑音増幅器

An X-band two-stage LNA, integrated with two HEMT's, four 10 pF-capacitors and a stage capacitor as lumped elements, is fabricated using a microstrip line structure. The circuit diagram and a photomicrograph are shown in Fig. 8. The intrinsic chip area is 0.80 mm $\times$ 0.78 mm, and is one-fourth that of conventional MMIC's. The first-stage HEMT has a source feedback inductance to achieve the optimum noise matching [14]. The matching network is designed employing 75 $\Omega$ microstrip lines and 70 $\Omega$ microstrip line for the source feedback inductance. Both transmission lines are formed on different dielectric layers to obtain a flexible layout. The measured and calculated characteristics of the two-stage amplifier are shown in Fig. 9. The noise performance of the fabricated amplifier is measured using an on-wafer probe station and an HP8970 noise figure meter. The amplifier shows a noise figure of 2.6-2.65 dB and a gain of 19.1-20.3 dB in the frequency range of from 11.7 GHz to 12.2 GHz, and its input VSWR and output VSWR are better than 1.6 and 1.4, respectively. The noise performance is slightly deteriorated by comparison with conventional MMIC's. Excess value of the noise figure caused by tramsmission line losses is approximately 0.95 dB at 12 GHz.

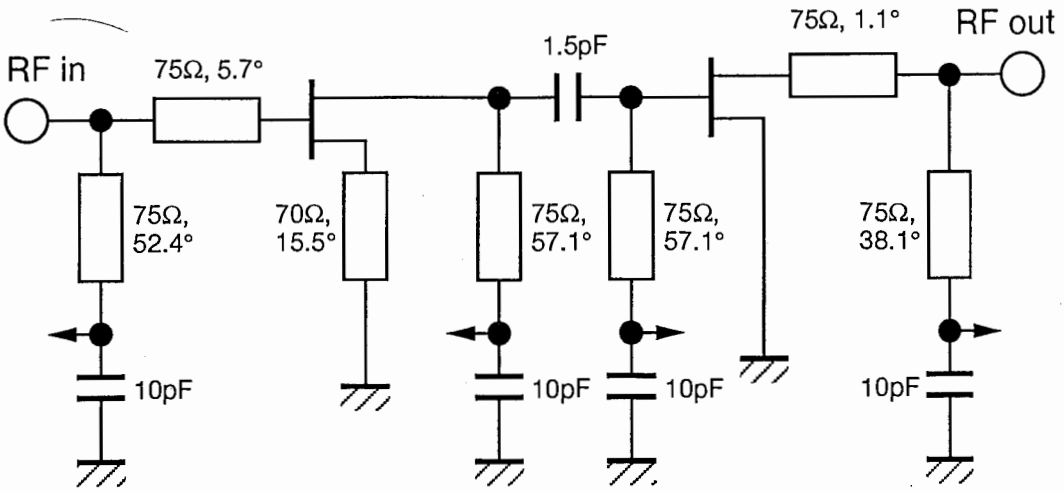


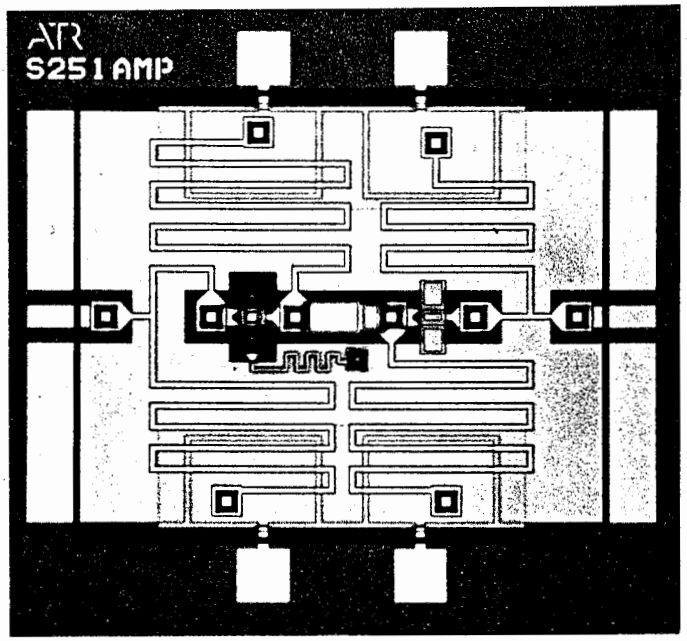


**Fig. 8** (a) Circuit diagram and (b) photomicrograph of an X-band LNA. The electrical lengths of the transmission lines are given at 12 GHz.

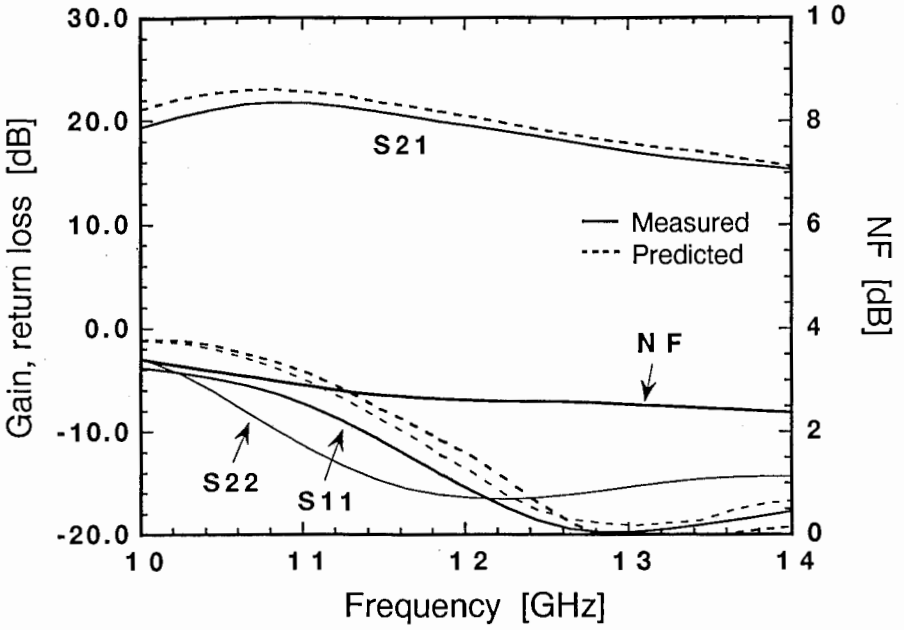


**Fig. 9** Characteristics of fabricated X-band LNA. ($Vds = 3\ V$, $Idss = 20\ mA$). Solid line: measured, dashed line: predicted.

### 2.4.2 広帯域増幅器

A Ka-band single-stage wideband amplifier is designed for a center frequency of 20 GHz. The circuit diagram and a photomicrograph of the amplifier are shown in Fig. 10. The impedance of the transmission lines is constrained to be within the range of from 20 Ω to 80 Ω, for the purposes of a reduced size and an acceptable transmission line loss. Low impedance, less than 30 Ω, transmission lines, which are difficult to utilize in conventional MMIC's, are chosen to achieve amplifier gain flatness in wideband. In this case, a triplate line is used as the 25 Ω transmission line, and a microstrip line is used as the 75 Ω transmission line. Fig. 11 shows the calculated and measured amplifier performance. The amplifier shows a gain of 8.0-9.5 dB in the frequency range of from 16.0 GHz to 26.5 GHz, and its input/output return losses are better than 8 dB at 26.5 GHz. Although the amplifier is designed using a single-stage HEMT configuration, wideband gain flatness is achieved. This amplifier circuit is applied to a unit-amplifier of a balanced amplifier as described below. The fabricated amplifier shows a noise figure of 4.6-5.2 dB, and its noise characteristics are slightly deteriorated due to lossy transmission lines. However, the chip size is very small, that is, 1.2 mm × 0.9 mm, while the intrinsic chip area is only 0.8 mm × 0.6 mm. Similarly, other types of amplifiers, whose bandwidth is relatively wide, are also designed within a 0.8 mm × 0.5 mm area, and show a gain of 6.0-8.5 dB in the frequency range of from 15.5 GHz to 33.5 GHz.

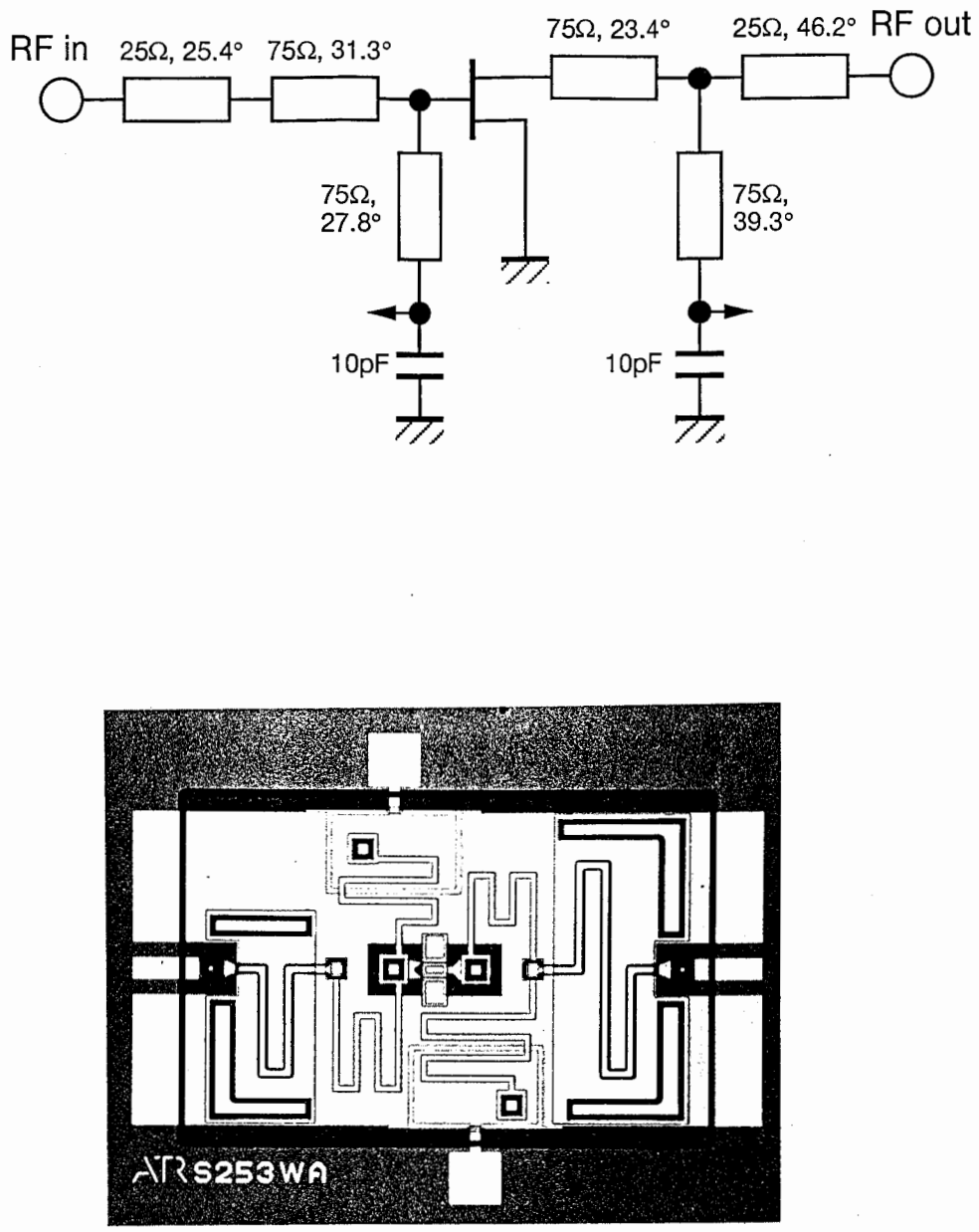


**Fig. 10** (a) Circuit diagram and (b) photomicrograph of a single-stage wide-band amplifier. The electrical lengths of the transmission lines are given at 20 GHz.

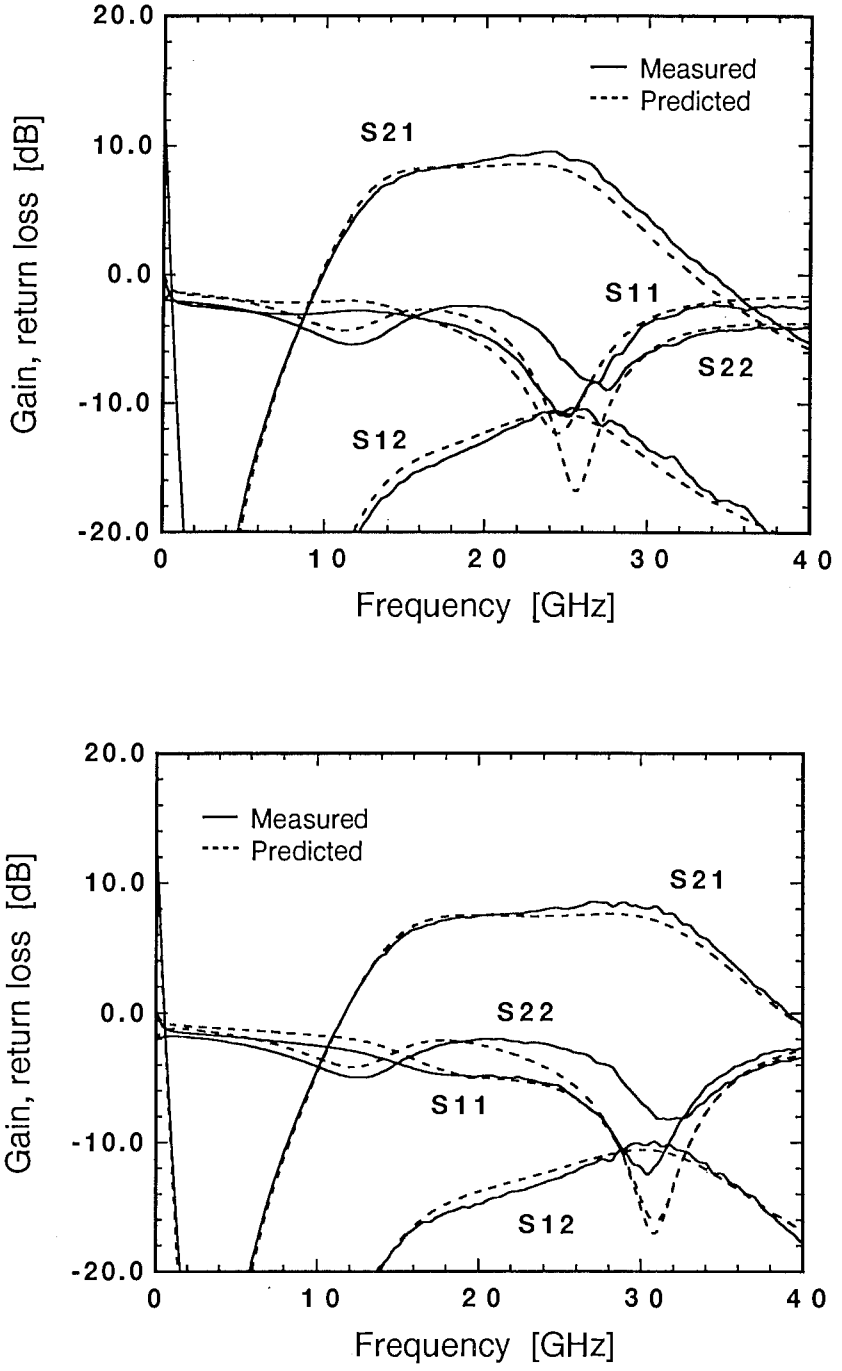


**Fig. 11** Characteristics of fabricated wideband amplifiers ($Vds = 3V$, $Idss = 20\ mA$). (a) A 16-26.5 GHz band amplifier and (b) a 15.5-33.5 GHz band amplifier. Solid line: measured, dashed line: predicted.

### 2.4.3 平衡型増幅器

To demonstrate the ability of the multilayer structure, we designed a balanced amplifier [15] at a center frequency of 20 GHz using branch-line hybrids, as 90-degree couplers, composed of a multilayer structure. A schematic cross sectional view of a multilayer structure and SEM photographs of a fabricated hybrid are shown in Fig. 12. The hybrid consists of 50 Ω microstrip lines and 35 Ω inverted microstrip lines whose polyimide film thickness is 5 $\mu$m, and the microstrip lines are fabricated over the inverted microstrip lines. Both transmission lines are isolated by the ground plane metal, which is formed on the center layer of the dielectric materials. In this structure, the coupling effect between both transmission lines is eliminated. The hybrid shows coupling losses of 5.5 dB ± 0.5 dB, return losses and isolation are better than 15 dB in the frequency range of 18 GHz to 21 GHz [7]. In addition, the intrinsic hybrid circuit area is less than 0.3 $mm^2$. The layout and circuit diagram of a unit-amplifier are the same manner as those of the wideband amplifier. The circuit diagram and a photomicrograph of a balanced amplifier MMIC are shown in Fig. 13. The intrinsic chip area is 1.09 mm × 1.54 mm, although the balanced amplifier is constructed with two branch-line hybrids and two amplifiers. Fig. 14 shows the measured and calculated characteristics of the balanced amplifier. The fabricated balanced amplifier has a gain of 5.5 dB with a 3 dB-bandwidth of 4 GHz, and its input/output return losses are better than 20 dB at a center frequency of 20 GHz. The gain is approximately 3 dB smaller than that of a unit-amplifier. To obtain improved performance without increasing the circuit area, it is necessary to reduce the excess cou-

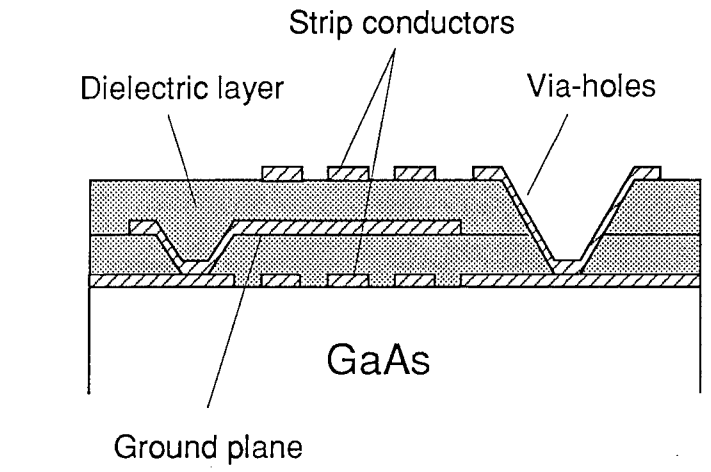


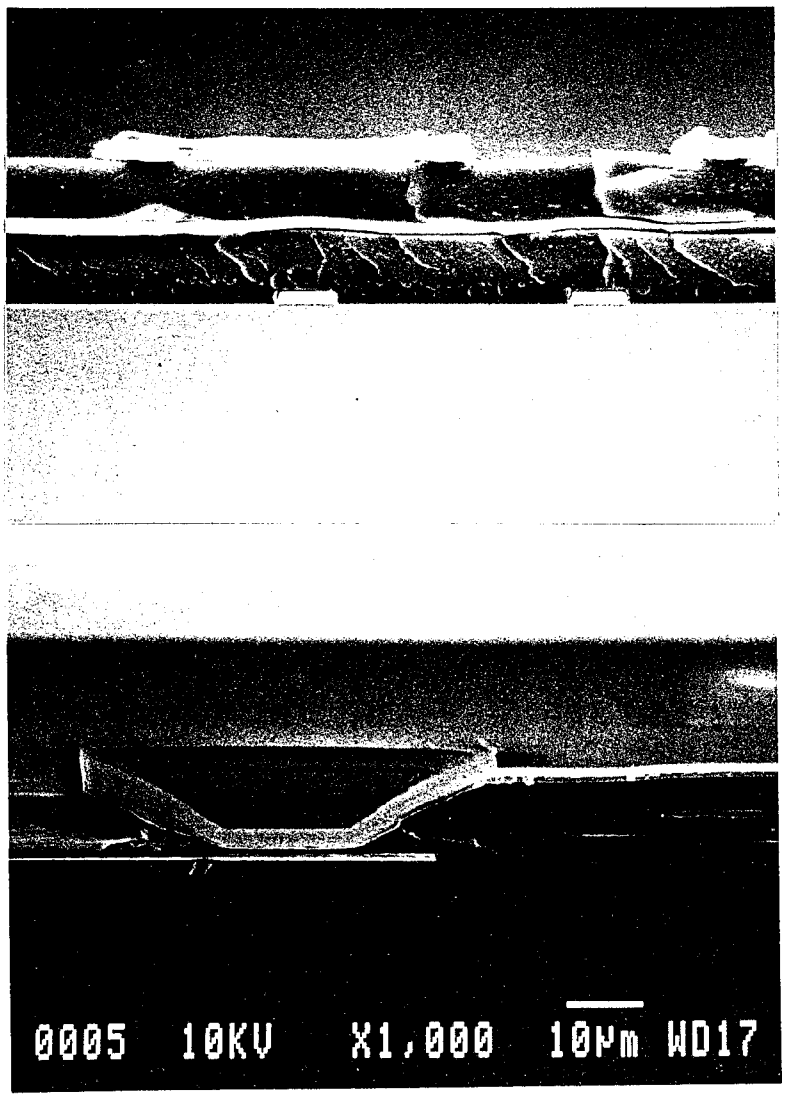


**Fig. 12** Multilayer transmission line structure using two dielectric layers. (a) Schematic cross section and (b) SEM photographs of a fabricated structure (multi-layered transmission lines and a via-hole view).

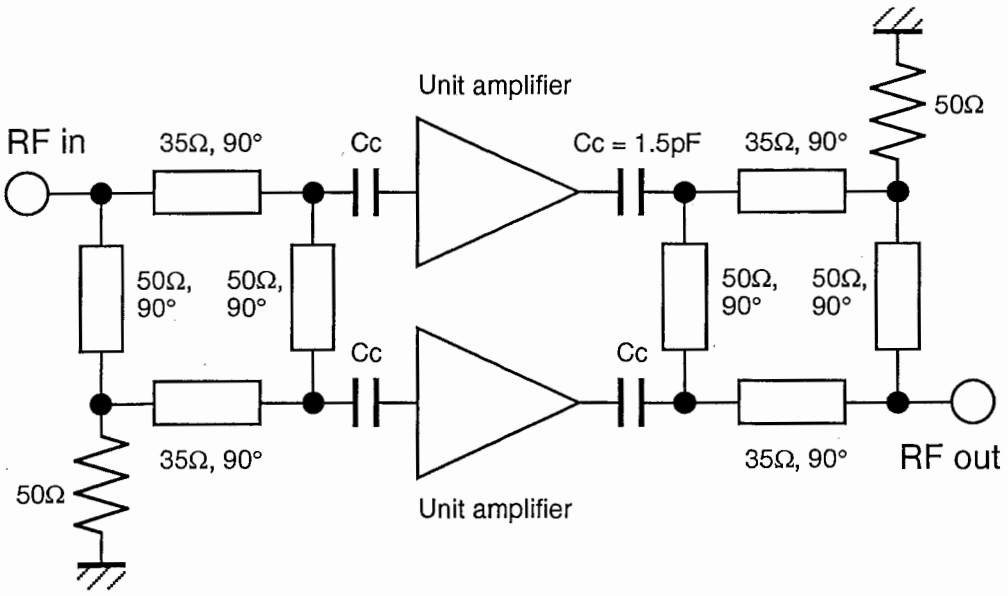


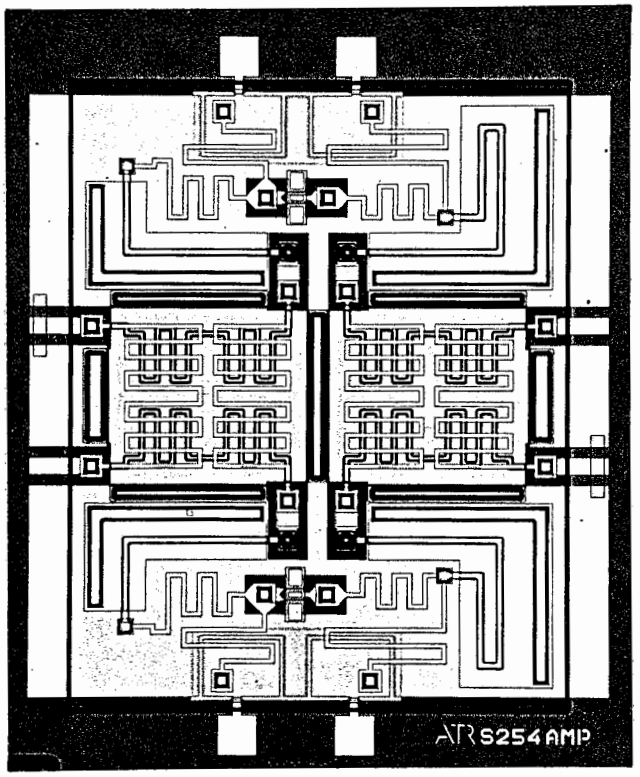


**Fig. 13** (a) Circuit diagram and (b) photomicrograph of a balanced amplifier. The electrical lengths of the transmission lines are given at 20 GHz.

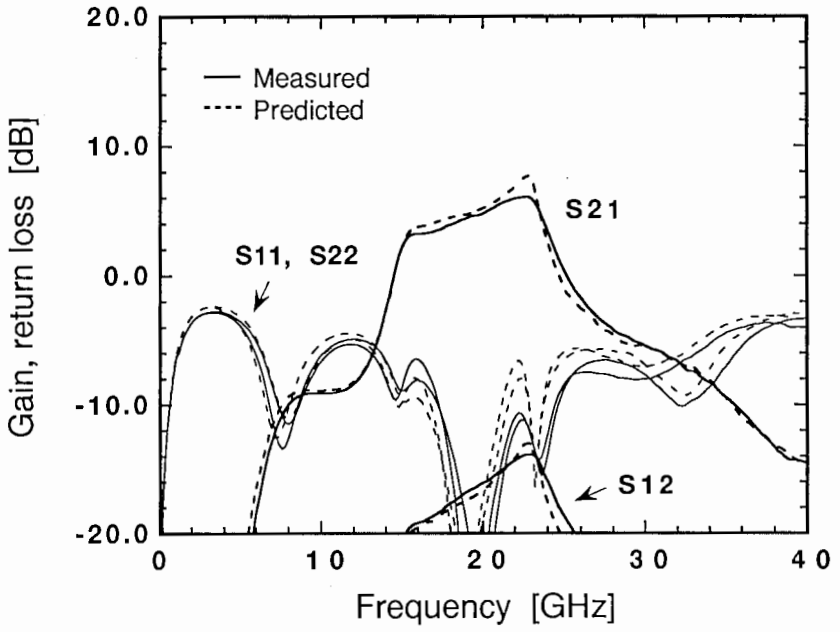


**Fig. 14** Characteristics of a fabricated balanced amplifier ($Vds = 3\ V$, $Idss = 20\ mA$). Solid line: measured, dashed line: predicted.

pling loss of the 90-degree hybrid. Investigations for new types of hybrids are in progress.

## 2.5 まとめ

Very small-sized MMIC amplifiers using thin film transmission line structures composed of thin dielectric layers on the GaAs wafer surface have been proposed, and their performance was demonstrated. The transmission line structures can be effectively combined with microwave active circuits. An X-band two-stage LNA, a Ka-band single-stage wideband amplifier and a balanced amplifier have been designed within very small areas, e.g., 0.63 $mm^2$, 0.48 $mm^2$ and 1.68 $mm^2$, respectively, while good performance has been maintained. The proposed amplifier configurations can be applied to high-density and multi-functional integration of MMIC modules.

## 参考文献


[1] J. Berenz, M. LaCon and M. Luong, "Single chip Ka-band transceiver," *IEEE MTT-S Int. Microwave Symp.*, pp. 517–520, June 1991.

[2] T. Hiraoka, T. Tokumitsu and M. Aikawa, "Very small wide-band MMIC magic-T's using microstrip lines on a thin dielectric film," *IEEE Trans. Microwave Theory and Tech.*, vol. **MTT-37**, pp.1569–1575, Oct. 1989.

[3] H. Nakamoto, T. Tokumitsu and M. Aikawa, "A monolithic, port-interchanged rat-race hybrid using a thin film microstrip line crossover," *19th European Microwave Conf.*, pp. 311–316, Sept. 1989.

[4] T. Tokumitsu, T. Hiraoka, H. Nakamoto and T. Takenaka, "Multilayer MMIC using a 3$\mu$m $\times$ 3-layer dielectric film structure," *IEEE MTT-S Int. Microwave Symp.*, pp. 831–834, May 1990.

[5] H. Ogawa, T. Hasegawa, S. Banba and H. Nakamoto, "MMIC transmission lines for multi-layered MMIC's," *IEEE MTT-S Int. Microwave Symp.*, pp. 1067–1070, June 1991.

[6] S. Banba, T. Hasegawa, H. Ogawa and T. Tokumitsu, "Novel MMIC transmission lines using thin dielectric layers," *IEICE Japan Trans. Electron.*, vol. **E75-C**, pp. 713–720, June 1992.

[7] S. Banba, T. Hasegawa and H. Ogawa, "Multilayer MMIC branch-line hybrid using thin dielectric layers," *IEEE Microwave and Guided Wave Lett.*, vol. **1**, pp. 346–347, Nov.

1991.

[8] T. Hirota, Y. Tarusawa and H. Ogawa, "Uniplanar MMIC hybrid - A proposed new MMIC structure," *IEEE Trans. Microwave Theory and Tech.,* vol. **MTT-35**, pp.576–581, June 1987.

[9] Y. Harada, F. Matsumoto and T. Nakakado, "A Novel polyimide film preparation and its preferential-like chemical etching techniques for GaAs device," *J. Electrochem. Soc.,* vol. **130**, pp.129–134, Jan. 1983.

[10] M. Matsuhara and T. Angkaew, "Analysis of waveguide with loss or gain by the Finite-Element-Method," *Trans. IEICE,* vol. **J71-C**, pp.1398–1403, Oct. 1988.

[11] K. C. Gupta, R. Garg and I. J. Bahl, *Microstrip Lines and Slotlines,* Artech House, 1979.

[12] R. A. Pucel, D. J. Masse and C. P. Hartwig, "Losses in microstrip," *IEEE Trans. Microwave Theory and Tech.,* vol. **MTT-16**, pp.342–350, June 1968.

[13] Y. Pastol, G. Arjavalingam, J. M. Halbout and G. V. Kopcsay, "Absorption and dispersion of low-loss dielectrics measured with microwave transient radiation," *Electron. Lett.,* vol. **25**, pp.523–524, April 1989.

[14] R. S. Engelbrecht and K. Kurokawa, "A wide-band low noise L-band balanced transistor amplifier," *Proc. IEEE,* vol. **53**, pp.237–247, March 1965.

[15] R. E. Lehmann and D. D. Heston, "X-band monolithic series feedback LNA," *IEEE Trans. Microwave Theory and Tech.,* vol. **MTT-33**, pp.1560–1566, Dec. 1985.

# 3 誘電体薄膜を用いた多層化MMIC方向性結合器

Low-loss and small-sized MMIC directional couplers utilizing a multi-layer structure composed of coupled thin film transmission lines on a GaAs wafer surface are newly proposed. The fundamental characteristics of the couplers are discussed through calculations by numerical analysis, and the performance of the couplers and an application to reverse-phase hybrid ring are demonstrated. The results show that a 3 dB-coupler can be designed within a 0.78 mm × 0.78 mm area for a center frequency of 20 GHz. Coupling losses of 3.7 dB ± 0.2 dB over a 4 GHz bandwidth and isolation of better than 28 dB in the frequency range of 0-30 GHz are achieved. The proposed coupler configurations can be applied to the high-density and multi-function integration of MMIC's.

## 3.1 はじめに

Directional couplers are important elements as 90-degree power dividers and power combiners in microwave circuits such as balanced amplifiers, balanced mixers and microwave signal processors. However, it is difficult to achieve tight coupling on microwave integrated circuits (MIC's). As an alternative, a branch-line hybrid constructed with four quarter-wavelength transmission lines can be employed as a 3 dB-coupler. Nevertheless, its use in monolithic microwave integrated circuits (MMIC's) is limited due to its large size. To design multi-function, high-density and cost-effective MMIC's, we must reduce the area of the hybrid.

Recently, a structure of thin film transmission lines, which utilize narrow width microstrip conductors on thin (several-$\mu$m thick) dielectric materials

fabricated over the ground metal on a GaAs wafer surface, was reported [1]-[7]. Thin film transmission lines allow for high-density circuit integration because of reduced transmission line widths and their ready application to multilayer configurations. In addition, meander-like and cross-over transmission line structures are easily fabricated in a small area. Therefore, a highly flexible circuit design can be achieved for a 3-dimensional structure; this configuration is suitable for high density integration of MMIC's. Thin film transmission lines can also be integrated within uniplanar circuits, and are normally called multilayer MMIC's.

The initial applications of such a structure were small-sized hybrid rings such as branch-line and rat-race hybrids [2], [4], [5]. Quasi-lumped-element hybrid rings, which utilize combinations of short high-impedance transmission lines and shunt-lumped capacitors, have also been reported [8]. Although these hybrids have substantially reduced occupied areas, their excess coupling losses become large due to lossy transmission lines, and it is difficult to obtain balanced port characteristics and wideband performance. Therefore, the performance of MMIC's using these hybrids are drastically deteriorated compared with those of conventional microwave circuits. It is necessary to achieve high-performance 90-degree hybrids without increasing the circuit area.

In this paper, the configurations of directional couplers utilizing thin dielectric layers fabricated on a GaAs wafer surface are proposed. The directional couplers are constructed with a multilayer structure consisting of coupled thin film transmission lines with a tuning septum and floating conductor. The fundamental characteristics of the directional couplers are calculated by the quasi-static finite-element-method (FEM) and full-wave FEM, and their

suitability for use in microwave circuits is discussed. The transmission line loss dominated by conductor loss is also discussed to predict the frequency characteristics of the couplers. Some advantages of the proposed directional couplers are as follows: (1) excellent performance and design accuracy, (2) small size for use in MMIC's, (3) good compatibility with coplanar MMIC's and (4) the possibility of loose coupling to tight coupling utilizing the same process. Finally, the design and performance of a 20 GHz tight coupler (such as $-3$ dB) and a medium coupler (such as $-6$ dB) are presented, and an application to a reverse-phase hybrid ring employed as a 180-degree hybrid is demonstrated.

## 3.2 方向性結合器の構成

The major problem in the directional couplers based on parallel-coupled transmission lines is realization of tight coupling. This problem can be solved by fabricating a floating potential conductor over a dielectric overlay to reduce the odd-mode impedance [9], or by using a ground conductor with a tuning septum to increase the transmission line impedance [10]. In order to achieve a tight coupler that can maintain a high performance and reduce its occupied area, we combine these methods and fabricate the structure on a GaAs wafer surface utilizing a multilayer MMIC process.

The multilayer structure consists of polyimide films for the thin dielectric layers and 1-$\mu$m-thick gold films for the conductor metals. The process for polyimide film preparation and subsequent chemical etching was described in [11]. This process can generate cone-shaped via-holes which connect the microstrip conductors on the upper dielectric layers with the input/output ports

and ground plane on the GaAs substrate. The relative dielectric constant and loss tangent of the polyimide film are 3.7 and 0.01 (10 MHz), respectively. A uniformity in the thickness of better than 1 % is obtained up to 10 $\mu$m. The measured stress of the polyimide film is a constant value of $-2.4\times10^8$ dyn/cm$^2$, and is one-tenth that of $Si_3N_4$ and $SiO_2$ films. Futhermore, the surface of the films, which are formed by spin-coating, is flat due to its high viscosity. These properties show that polyimide film is a suitable dielectric material for multilayer MMIC fabrication. In our fabrication, the multilayer structure consists of four 2.5-$\mu$m-thick polyimide films; therefore, conductors can be formed up to five layers.

Cross-sectional views of multilayer MMIC directional couplers are shown in Figs. 15(a) (normal type) and (b) (inverted type). The directional couplers are constructed with coupled microstrip lines, a ground conductor with a tuning septum and floating conductor located over the microstrip lines. Each conductor is formed on a different dielectric layer. Since the floating conductor is located symmetrically over the microstrip lines, it works as a cold-wall (ground plane) in the odd-mode. In the even-mode, the potential of the floating conductor becomes close to that of the coupled microstrip lines, because the even-mode characteristics should not be changed substantially by the presence of the floating conductor. In the design, the even- and odd-mode characteristics in the coupled section must be evaluated. The characteristic impedance and guided wavelength of each mode are calculated by quasi-static FEM. Because these structures are small in comparison to the guided wavelength, quasi-TEM wave approximation can be used for numerical analysis. The desired coupling C and transmission line impedance $Z_0$ are written by

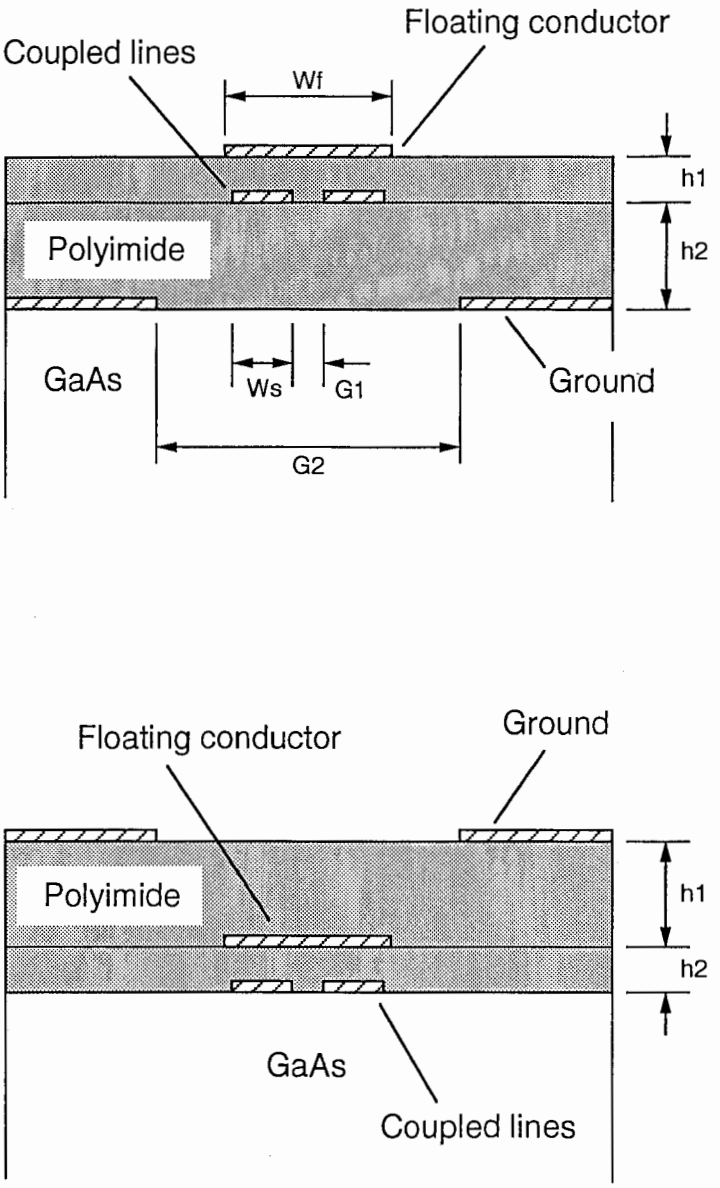


**Fig. 15** Cross-sectional views of multilayer MMIC directional couplers. (a) Normal type and (b) inverted type.

the following equations.

$$C = 20\log\left(\frac{Z_{even} - Z_{odd}}{Z_{even} + Z_{odd}}\right) \tag{7}$$

$$Z_0 = \sqrt{Z_{even} Z_{odd}} \tag{8}$$

where $Z_{even}$ and $Z_{odd}$ are the even-mode impedance and odd-mode impedance, respectively. In an inhomogeneous medium, the coupling length $L_c$ is determined by the mean of the even-mode and odd-mode quarter wavelengths.

$$L_c = \frac{1}{4} \cdot \frac{\lambda_{even} + \lambda_{odd}}{2} \tag{9}$$

To calculate the circuit performance, we simulate the frequency characteristics of the transmission line attenuation with a commercially-available CAD software package that includes user defined function routine (Touchstone). The frequency characteristic of the total attenuation per unit length $\alpha(f)$ is given by the following equation.

$$\alpha(f) = \alpha_c(F) \cdot \sqrt{\frac{f}{F}} \cdot \frac{1 - e^{-tK\sqrt{F}}}{1 - e^{-tK\sqrt{f}}} + \alpha_d(F) \cdot \frac{f^2}{F^2} \qquad [dB/mm], \tag{10}$$

where $F$ (in our case : $F = 20$ GHz) is the design frequency, and $\alpha_c(F)$ and $\alpha_d(F)$ are the conductor loss and dielectric loss at the design frequency, respectively. The $t$ and $K$ are conductor thickness and material constant $(= \sqrt{\pi\sigma\mu})$, respectively. Fig. 16 shows the calculated and measured characteristics of a 50 $\Omega$ microstrip line structure. A good agreement between these values is obtained in the frequency range of 0-40 GHz using(10). Therefore, this equation can be applied to coupling loss evaluation. The conductor losses of the directional coupler, which dominate in the odd-mode, are calculated by the full-wave FEM [12] at the design frequency of 20 GHz. In our calculation, the skin effect is considered, because the conductor thickness is approximately

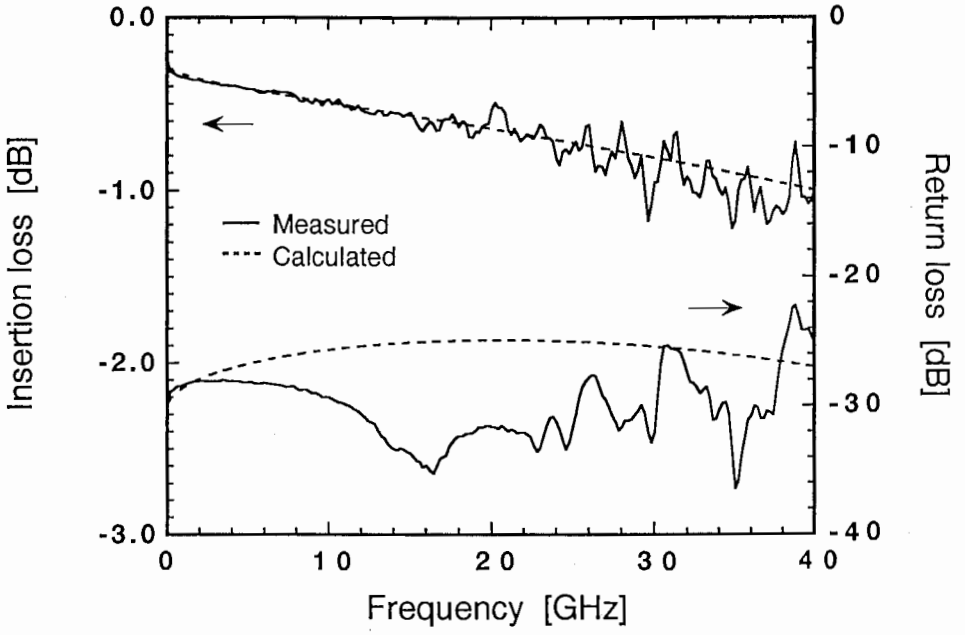


**Fig. 16** Calculated and measured frequency characteristics of a 50 Ω microstrip line. Solid line: measured, dashed line: calculated.

two times greater than the skin depth of the conductor at 20 GHz. The surface resistivity of the conductors and loss tangent of the polyimide films at 20 GHz are assumed to be 4.6 $\times 10^{-6}$ $\Omega \cdot m$ and 0.02, respectively. We also assume the surface roughness of the conductors to be zero, from observations by scanning electron microscopy (SEM).

### 3.3 方向性結合器の設計

Fig. 17 shows the calculated characteristic impedance and normalized guided wavelength of normal-type couplers in the even- and odd-modes as a function of tuning septum width, when the polyimide film thicknesses are $h1 = 2.5$ $\mu$m and $h2 = 7.5$ $\mu$m, respectively. To simplify the design and pattern layout, the distance between microstrip lines and width of the floating conductor are kept as $G1 = 10$ $\mu$m and $Wf = G1 + 2Ws + 4$ $\mu$m, respectively. The even-mode characteristics are strongly dependent on the tuning septum. For example, the even-mode impedance of these coupled transmission lines, whose tuning septum widths range from 40 $\mu$m to 200 $\mu$m, are between 70 $\Omega$ and 150 $\Omega$, when the microstrip conductor width is 15 $\mu$m. On the other hand, the odd-mode characteristics have little effect on the tuning septum. To achieve a 3 dB-coupler with 50 $\Omega$-impedance, the widths of the microstrip line and tuning septum are $Ws = 15$ $\mu$m and $G2 = 110$ $\mu$m, respectively. The polyimide film thickness dependence is shown in Fig. 18. The ratio of even- to odd-mode impedance becomes small with increasing distance between floating conductor and microstrip lines; it becomes large with increasing microstrip width.

Directional couplers based on parallel-coupled transmission lines using an in-

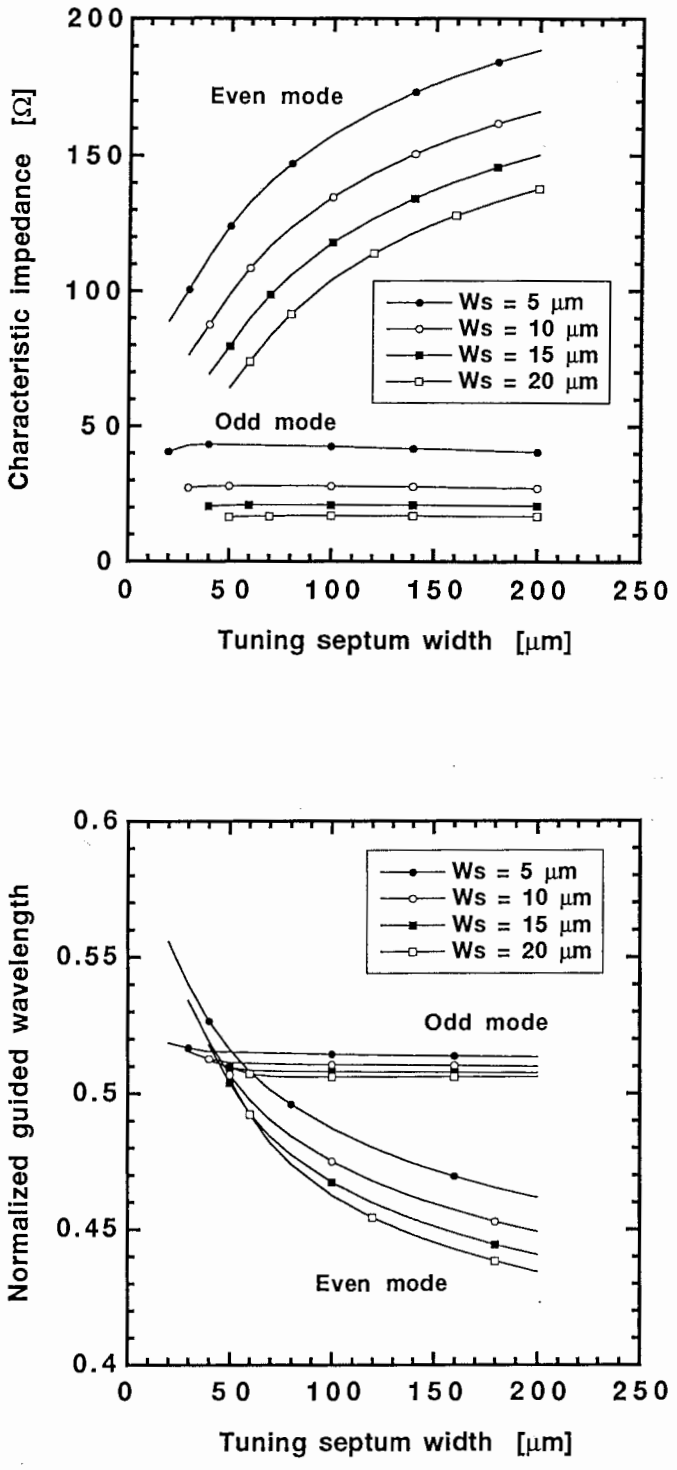


**Fig. 17** (a) Calculated characteristic impedance and (b) normalized guided wavelength of normal-type structures, as a function of tuning septum width.

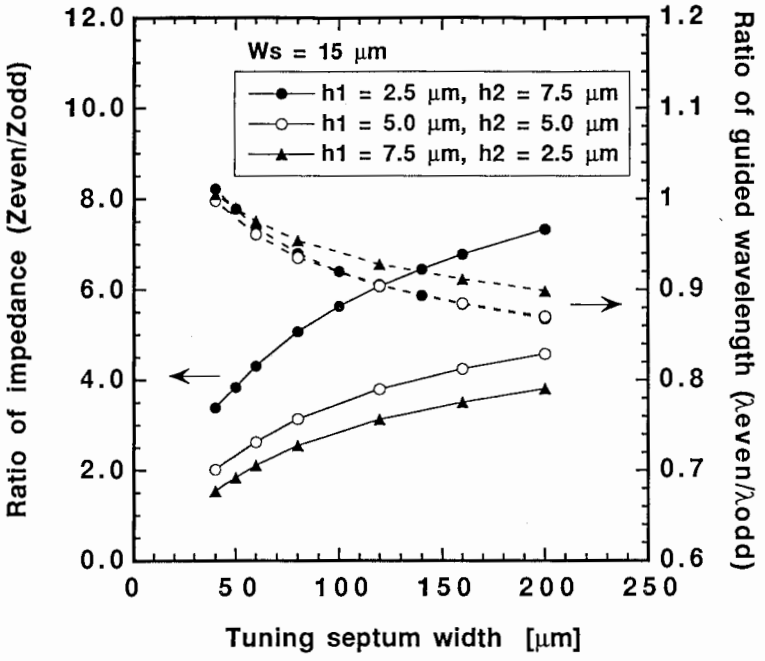


**Fig. 18** Polyimide film thickness dependence of the ratio of even- and odd-mode impedance and guided wavelength.

homogeneous medium have different guided wavelengths in each mode. In general, the effective dielectric constant in the even-mode becomes larger than that in the odd-mode, and this phenomenon is emphasized for tight couplings. The difference in guided wavelengths degrades the coupler performance. The inverted-type coupler has a different arrengement of conductors as shown in Fig. 15(b). The coupled microstrip lines are formed on the GaAs wafer surface, and the ground plane is formed over the dielectric layers. In this structure, the effective dielectirc constant in the odd-mode can be increased, because the electric field concentrates near the GaAs substrate. In addition, the effective dielectric constant in the even-mode is not substantially increased. Therefore, the inverted-type coupler can achieve tight coupling while maintaining the even- and odd-mode velocity matching. The calculated characteristic impedance and normalized guided wavelength of inverted-type couplers are shown in Fig. 19. The inverted-type couplers show relatively small even- and odd-mode impedances; however, the difference in guided wavelengths in each mode becomes small compared with that of the normal-type couplers. For example, the ratio of guided wavelength ($=\lambda_{even}/\lambda_{odd}$) becomes 0.966 in an inverted 3 dB-coupler, while the ratio becomes 0.912 for the normal type (*See Table 2*).

Table 2 summarizes the structural parameters and calculated characteristics of several coupled sections. The widths of the microstrip lines and tuning septum become large in the design of 3 dB-couplers with increasing $h1$, and the even- and odd-mode velocity ratios are not well matched. This results in a degradation of the wideband performance; however, the conductor losses in the odd-mode become smaller than that of others. Therefore, the structures

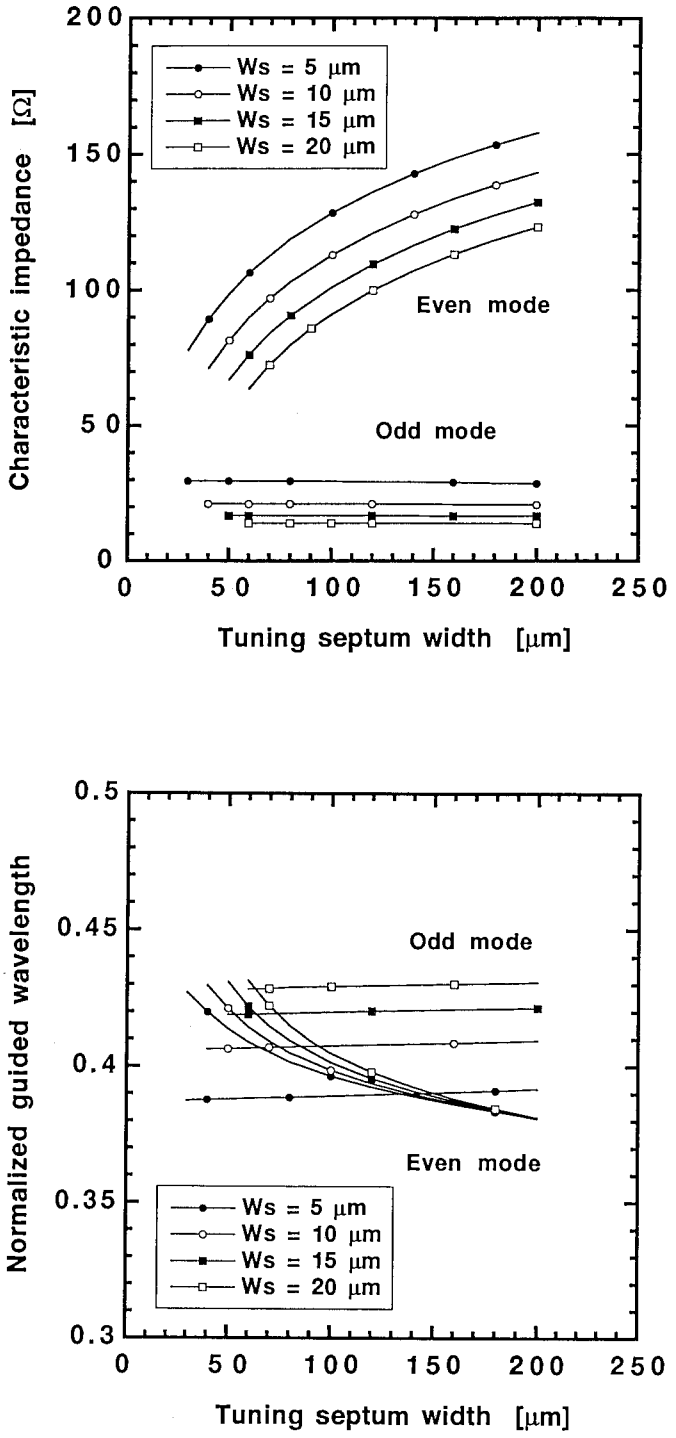


**Fig. 19** (a) Calculated characteristic impedance and (b) normalized guided wavelength of inverted-type structure, as a function of tuning septum width.

**Table 2** Structural parameters and calculated even- and odd-mode characteristics of several coupled sections (*: inverted type structure). The conductor losses are calculated at 20 GHz.

| | Structural parameters [μm] | | | | Calculated characteristics | | | | | | |
|---|---|---|---|---|---|---|---|---|---|---|---|
| | | | | | Coupling [dB] | Characteristic impedance [Ω] | | Effective dielectric constant | | Conductor loss [dB/mm] | |
| | h1 | h2 | Ws | G2 | | Even | Odd | Even | Odd | Even | Odd |
| (1) | 2.5 | 7.5 | 15 | 110 | -2.99 | 122.6 | 20.9 | 4.657 | 3.876 | 0.251 | 0.808 |
| (2) | 5.0 | 5.0 | 27 | 220 | -3.01 | 120.6 | 20.7 | 5.962 | 4.302 | 0.241 | 0.464 |
| (3)* | 7.5 | 2.5 | 10 | 120 | -3.05 | 120.9 | 21.0 | 6.450 | 6.013 | 0.421 | 1.105 |
| (4) | 2.5 | 7.5 | 10 | 40 | -5.70 | 87.4 | 27.7 | 3.711 | 3.806 | 0.324 | 0.788 |
| (5) | 5.0 | 5.0 | 16 | 70 | -6.18 | 86.3 | 29.5 | 4.723 | 4.230 | 0.262 | 0.462 |

**Table 3** Structural parameters and calculated characteristics of thin film transmission lines for use in a multilayer branch-line hybrid. The conductor losses are calculated at 20 GHz.

| Transmission line structure | Structural parameters [μm] | | Calculated characteristics | | |
|---|---|---|---|---|---|
| | Polyimide thickness | Line width | Characteristic impedance [Ω] | Effective dielectric constant | Conductor loss [dB/mm] |
| Microstrip line | 5.0 | 10 | 50.1 | 2.870 | 0.398 |
| Inverted microstrip line | 5.0 | 10 | 35.0 | 5.962 | 0.590 |

**Table 4** Calculated performance of 3 dB-couplers and a multilayer branch-line hybrid.

| Structure | Calculated results [dB] | | |
|---|---|---|---|
| | Coupling losses | Return loss | Isolation |
| 3 dB-coupler (1) | $3.75 \pm 0.05$ | $> 26$ | $> 26$ |
| 3 dB-coupler (2) | $3.6 \pm 0.1$ | $> 23$ | $> 22$ |
| 3 dB-coupler (3) | $3.95 \pm 0.05$ | $> 29$ | $> 29$ |
| Multilayer branch-line | $5.4 \pm 0.2$ | $> 17$ | $> 15$ |

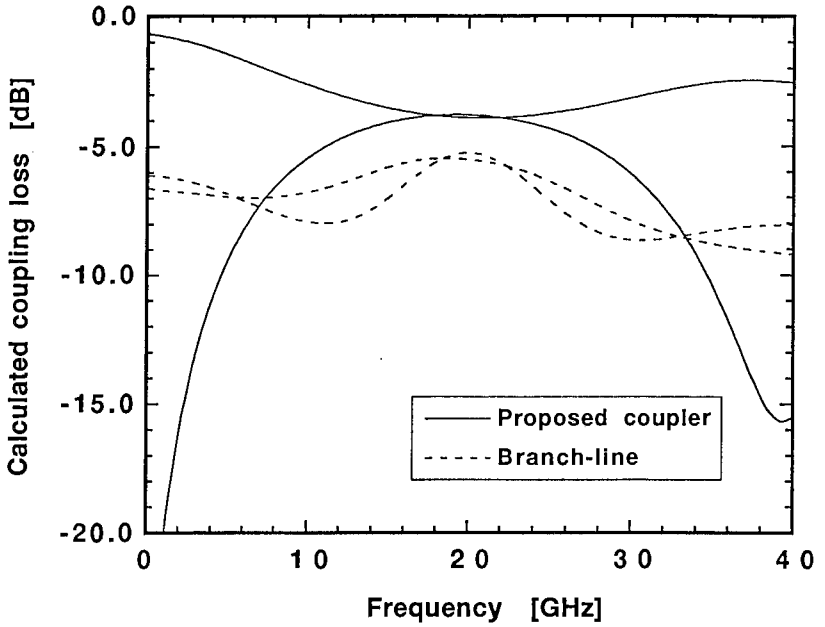


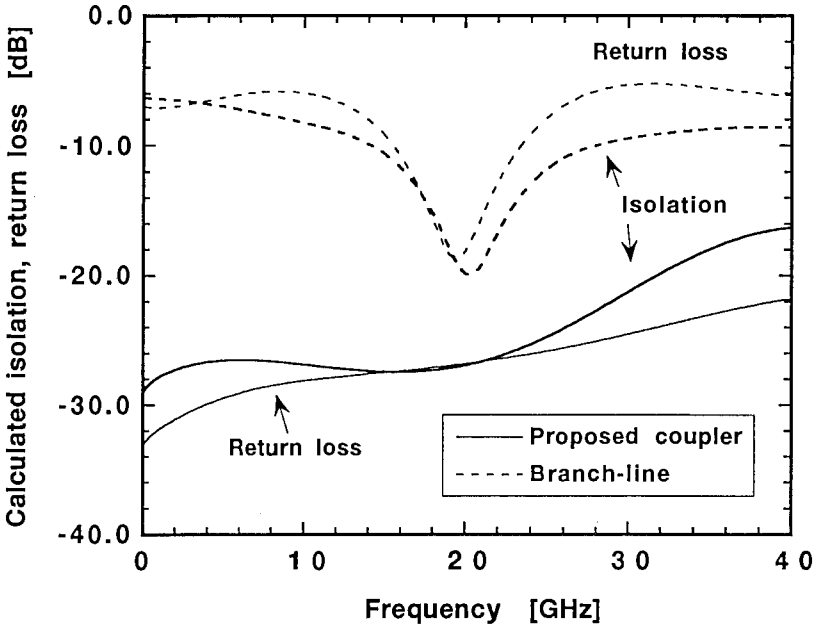


**Fig. 20** Performance comparison of a 3 dB-coupler and branch-line hybrid. (a) Coupling losses and (b) return loss and isolation.

are suitable for medium and tight couplers with low-loss. To compare the performance, we simulate the characteristics of the proposed coupler and the multilayer branch-line hybrid reported in [4], using values from Tables 2 and 3. The calculated coupling losses, return loss and isolation of the circuits are summarized in Table 4. Moreover, the frequency characteristics of a 3 dB-coupler and the hybrid are shown in Fig. 20. Although both circuits employ thin film transmssion line structures, the coupling losses of the proposed coupler are approximately 1.8 dB smaller than those of the hybrid ring at a center frequency of 20 GHz. This is caused by the usage of four quarter-wavelength transmission lines in the hybrid ring. By reducing the total transmission line length, we can obtain excellent performance within a small area.

On the basis of the calculations, it is easy to determine the widths of the coupled microstrip lines and location of the floating conductor corresponding to the odd-mode characteristics, and the tuning septum in the ground conductor corresponding to the even-mode characteristics. In addition, the proposed configurations have excellent design flexibility, since various structures can be fabricated utilizing a multilayer MMIC process. For example, a loose coupling of less than $-30$ dB can be obtained by removing the floating conductor and tuning septum, and by using a structure of coupled triplate lines.

### 3.4 特性

A 3 dB-coupler (type (a) in Table 2) is designed for a center frequency of 20 GHz and fabricated on a GaAs wafer surface. A microphotograph of the fabricated coupler is shown in Fig. 21. The chip size is very small, e.g., 1.1 mm $\times$ 1.1 mm including CPW input/output ports for measurements.

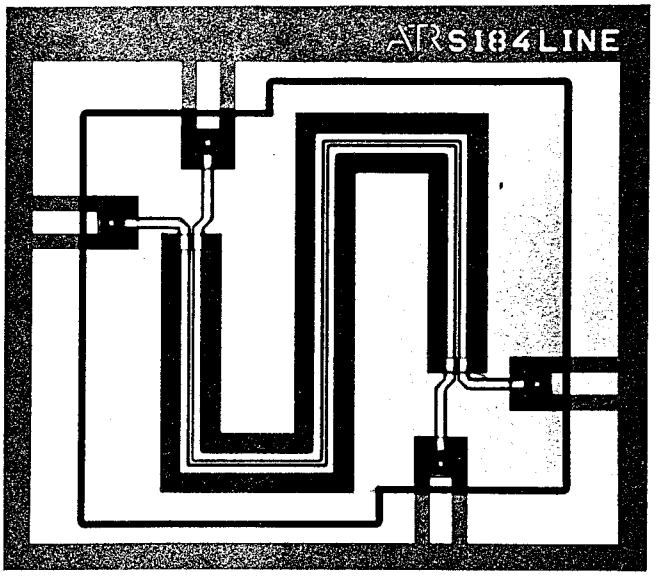


**Fig. 21** Microphotograph of a fabricated 3 dB-coupler.

The coupling length of the structure is 1820 $\mu$m, and coupled section has a meander-like configuration to reduce the circuit area. Each microstrip conductor is connected to the CPW input/output ports on the GaAs wafer surface through via-holes (15 $\mu$m $\times$ 15 $\mu$m). The couplers are tested using on-wafer probes and an HP8510B network analyzer. Termination-probes, whose return losses are better than 20 dB up to 40 GHz, are also used. Frequency characteristics of the coupler are shown in Figs. 22(a) through 22(c). The calculated values are also plotted in the figures including discontinuities in the transition regions between the coupled sections and input/output ports. The coupler shows coupling losses of within 3.7 dB $\pm$ 0.2 dB, and the phase difference between coupling-port and through-port is $91° \pm 1°$ in the frequency range of 18-22 GHz. Furthermore, isolation is better than 28 dB and return losses are better than 22 dB in the frequency range of 0-30 GHz. Excellent performance is obtained, while the chip size is similar to those of previous reports [4], [8]. The directional coupler can be applied to balanced amplifiers and image-rejection mixers with no degradation in circuit performance and increase in circuit area. A 6 dB-coupler is also fabricated and measured. A microphotograph and measured characteristics of a fabricated 6 dB-coupler are shown in Figs. 23 and 24, respectively. Coupling loss of 6.8 dB $\pm$ 0.2 dB, return losses of better than 22 dB and isolation of better than 25 dB are obtained in the frequency range of 18-22 GHz.

In general, a rat-race hybrid, which is constructed with one 3/4-wavelength and three 1/4-wavelength transmission lines, is employed as a 180-degree coupler in microwave circuits. However, such a hybrid using thin film transmssion lines shows unbalanced port characteristics and a relatively large insertion loss

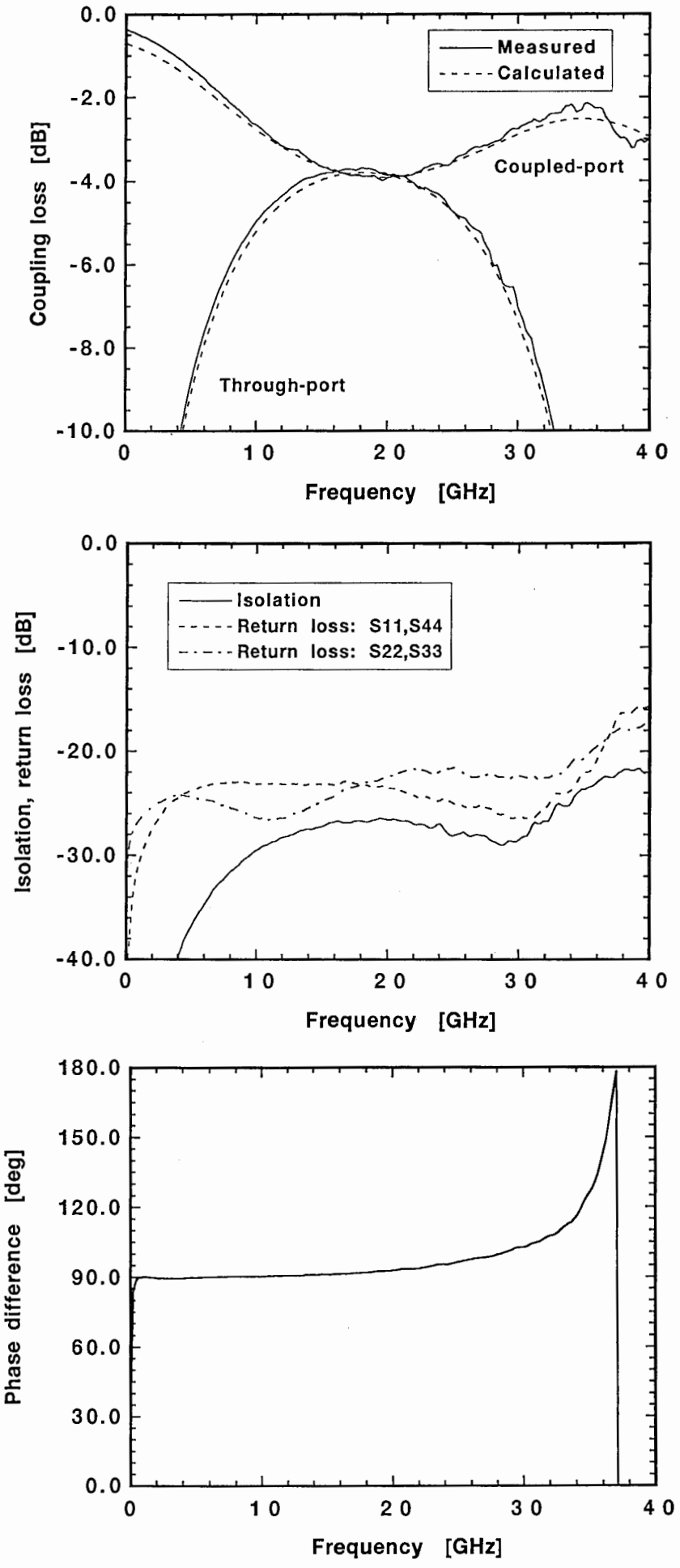


**Fig. 22** Measured characteristics of a fabricated 3 dB-coupler. (a) Coupling losses, (b) return losses and isolation and (c) phase difference.

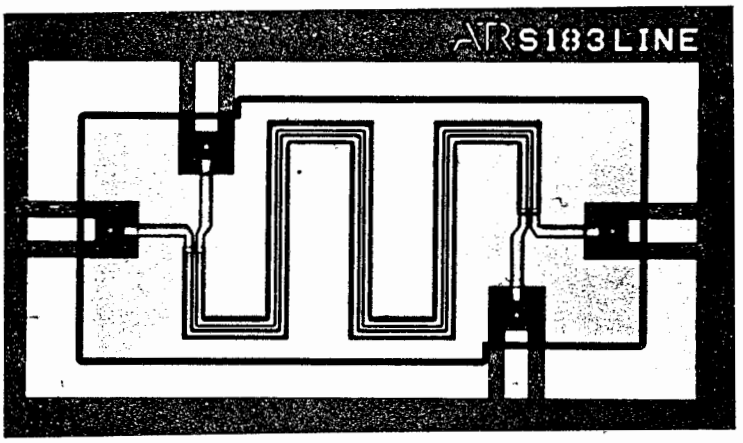


**Fig. 23** Microphotograph of a fabricated 6 dB-coupler.

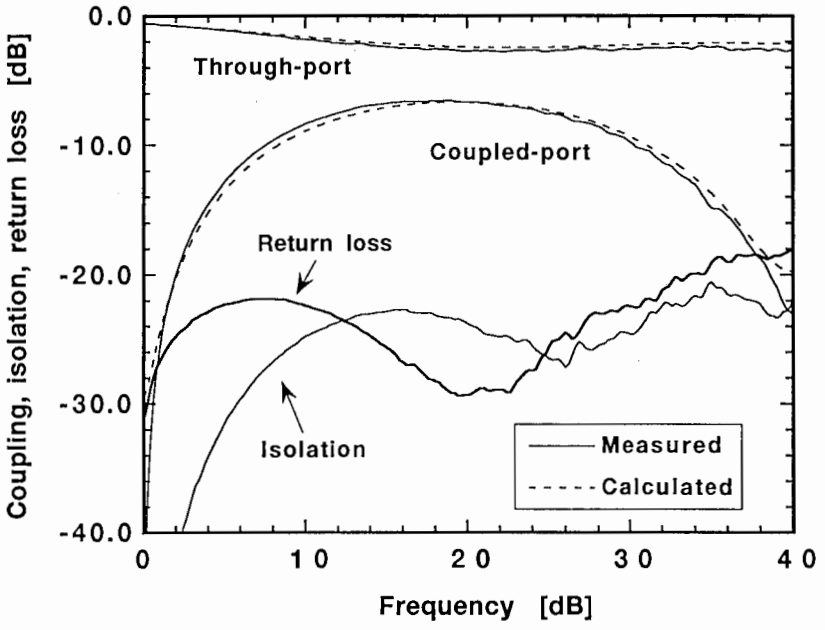


**Fig. 24** Measured characteristics of a fabricated 6 dB-coupler.

because of the 3/4-wavelength line whose loss is three times that of the others. To solve these problems and to demonstrate the ability of multilayer MMIC structures, we design a reverse-phase hybrid ring [14] replacing the 3/4-wavelength line of the rat-race hybrid with a 1/4-wavelength coupled section. The circuit diagram and measured characteristics are shown in Figs. 25 and 26, respectively. The intrinsic chip area is 2.3 mm × 0.5 mm. The hybrid ring consists of one coupled section ($Z_{even} = 159\ \Omega, Z_{odd} = 27\ \Omega$) and three 70 Ω transmission lines. All microstrip conductors are formed on the same dielectirc layer to avoid junction discontinuities. The hybrid ring shows measured coupling losses of within 5.3 dB ± 0.5 dB. Return losses and isolation are better than 17 dB and 20 dB, respectively, in the frequency range of 18-22 GHz. Good performance is obtained using the proposed coupler configurations. Phase conditions in the out-of-phase and in-phase operations are 170° ± 5° and 5° ± 2°, respectively. The differences from ideal performance are caused by parastic inductors between the coupled section and short-end.

### 3.5 まとめ

Small-sized multilayer MMIC directional couplers using coupled thin film transmssion line structures composed of thin dielectric layers on a GaAs wafer surface have been proposed, and their performance and application have been demonstrated. 20 GHz-band couplers have been designed within small areas, less than 1.0 $mm^2$, while excellent performance has been maintained. The proposed coupler configurations can be applied to the high-density and multifunction integration of MMIC modules such as balanced circuits and RF signal processing circuits.

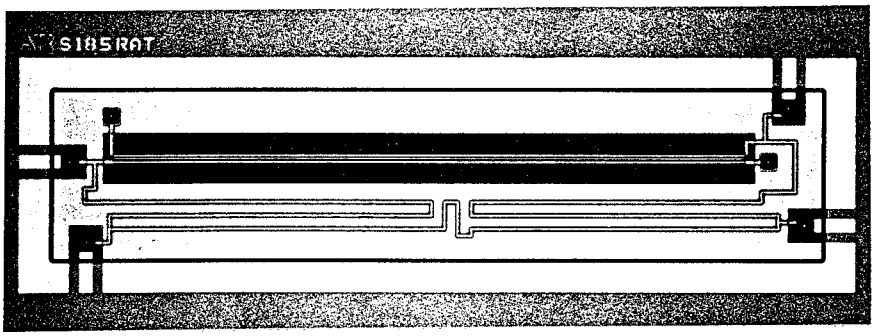


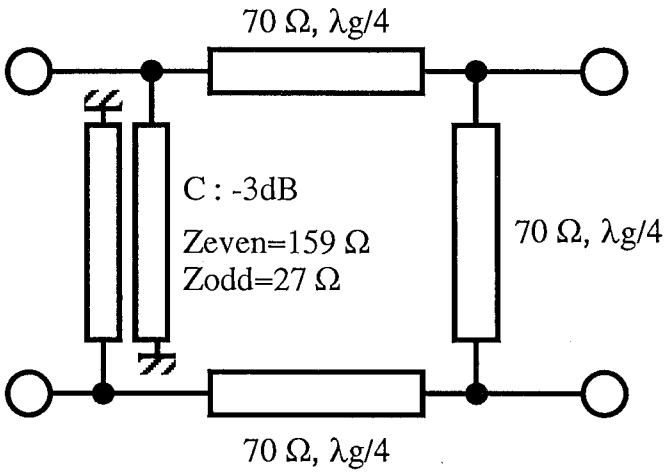


**Fig. 25** Circuit diagram of a reverse-phase hybrid ring.

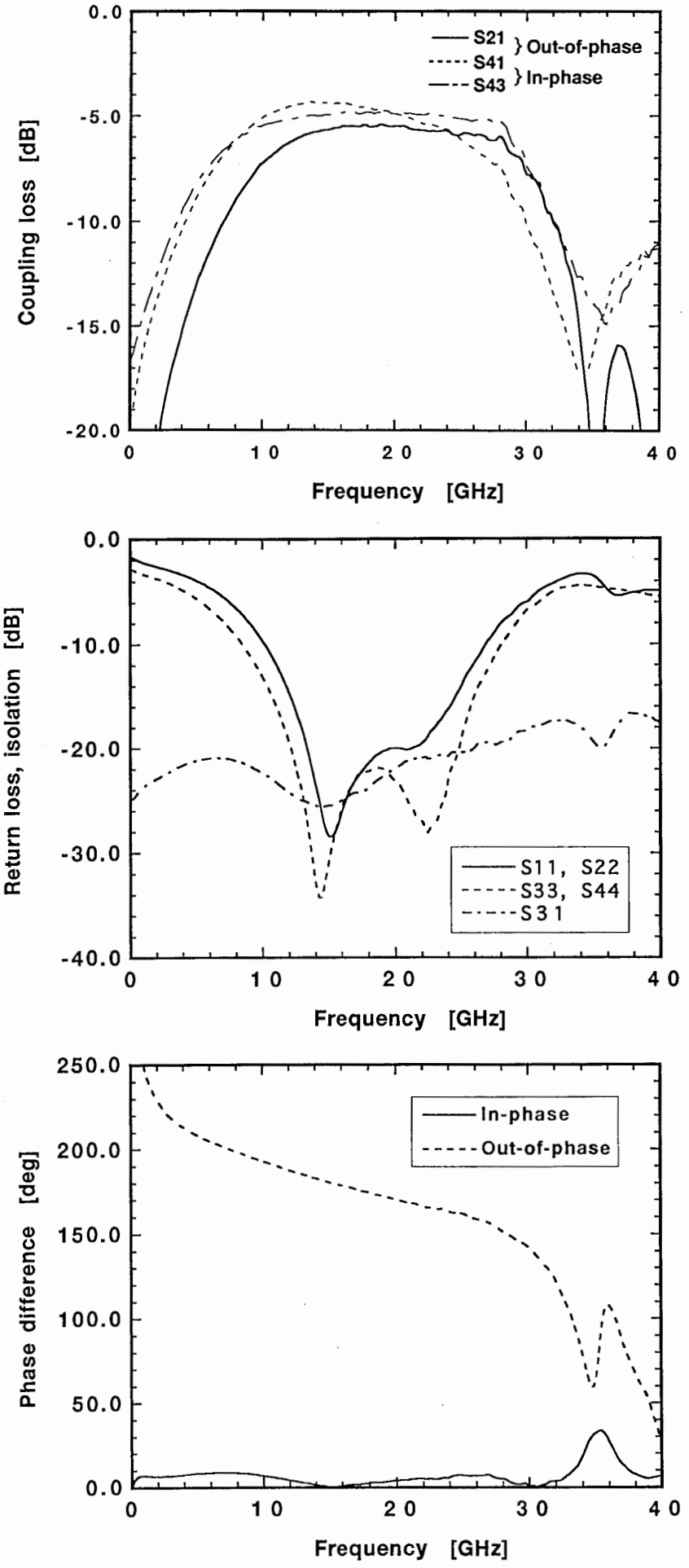


**Fig. 26** Measured characteristics of a fabricated reverse-phase hybrid ring. (a) Coupling losses, (b) return losses and isolation and (c) phase differences.

## 参考文献


[1] T. Hiraoka, T. Tokumitsu and M. Aikawa, "Very small wide-band MMIC magic-T's using microstrip lines on a thin dielectric film," *IEEE Trans. Microwave Theory and Tech.*, vol. **MTT-37**, pp. 1569–1575, 1989.

[2] H. Nakamoto, T. Tokumitsu and M. Aikawa, "A monolithic, port-interchanged rat-race hybrid using a thin film microstrip line crossover," *19th. European Microwave Conf.*, pp. 311–316, 1989.

[3] T. Tokumitsu, T. Hiraoka, H. Nakamoto and T. Takenaka, "Multilayer MMIC using a 3 $\mu$m $\times$ 3-layer dielectric film structure," *IEEE MTT-S Int. Microwave Symp.*, pp. 1067–1070, 1990.

[4] S. Banba, T. Hasegawa and H. Ogawa, "Multilayer MMIC branch-line hybrid using thin dielectric layers," *IEEE Microwave and Guided Wave Lett.*, vol. **1**, pp. 346–347, Nov. 1991.

[5] I. Toyoda, T. Hirota, T. Hiraoka and T. Tokumitsu, "Multilayer MMIC branch-line coupler and broad-side coupler," *IEEE Microwave and Millimeter-Wave Monolithic Circuits Symp.*, pp. 79–82, 1992.

[6] H. Ogawa, T. Hasegawa, S. Banba and H. Nakamoto, "MMIC transmission lines for multi-layered MMIC's," *IEEE MTT-S Int. Microwave Symp.*, pp. 1067–1070, June 1991.

[7] S. Banba, T. Hasegawa, H. Ogawa and T. Tokumitsu, "Novel MMIC transmission lines using thin dielectric layers," *IEICE Japan Trans. Electron.*, vol. **E75-C**, pp. 713–720, June 1992.

[8] T. Hirota, A. Minakawa and M. Muraguchi, "Reduced-size branch-line and rat-race hybrid for uniplanar MMIC's," *IEEE Trans. Microwave Theory and Tech.*, vol. **MTT-38**, pp. 270–275, 1990.

[9] K. Sachse, "A wide-band 3-dB coupler with a very tightly coupled cross-section of microstrip lines," *3rd. European Microwave Conf.*, **B.4.4**, 1973.

[10] R. K. Hoffmann, *Handbook of Microwave Integrated Circuits*, Artech House,1987.

[11] Y. Harada, F. Matsumoto and T. Nakakado, "A Novel polyimide film preparation and its preferential-like chemical etching techniques for GaAs device," *J. Electrochem. Soc.*, vol. **130**, pp. 129–134, Jan. 1983.

[12] M. Matsuhara and T. Angkaew, "Analysis of waveguide with loss or gain by the Finite-Element-Method," *Trans. IEICE Japan Trans. Electron.*, vol. **J71-C**, pp. 1398–1403, Oct. 1988 *(Japanese)*.

[13] Y. Pastol, G. Arjavalingam, J. M. Halbout and G. V. Kopcsay, "Absorption and dispersion of low-loss dielectrics measured with microwave transient radiation," *Electron. Lett.*, vol. **25**, pp. 523–524, April 1989.

[14] S. March, "A wideband stripline hybrid ring," *IEEE Trans. Microwave Theory and Tech.*, vol. **MTT-16**, pp. 361, 1968.

提案する光ファイバミリ波通信ネットワークでは、無数の超小型移動端末器を制御するためにピコセルゾーンを形成し、多数の無線基地局を配置することになる。この無線基地局には光およびミリ波信号の処理機能および、小型化・低コスト化が要求され、従来の光電子集積回路（ＯＥＩＣ）では対応できなくなる。新しい集積回路の考え方が必要になる。その一手段として、マイクロ波能動素子（例えば、ＨＥＭＴ、ＨＢＴ）を光制御マイクロ波素子として利用する光マイクロ波集積回路を提案した。以下に、ＨＥＭＴ光検出器を用いた光ファイバリンクの伝送特性とＭＭＩＣ化光受信器について述べ、また、光集積回路では分岐型光導波路の小型化に関して述べる。本提案は高機能な外部変調器や光ビームフォーミング等に適用できる。

## 4　光ファイバリンクにおけるＨＥＭＴ光検出器の伝送特性

A monolithic integrable HEMT photodetector is experimentally investigated for use in fiber optic subcarrier transmission links. The frequency response and noise performance of the HEMT photodetector are discussed in this paper. The results include a response of 1.0 A/W and a signal-to-noise ratio of 49.8 dB (BW = 1 MHz, Popt = −8.5 dBm), at a subcarrier frequency of 1 GHz. This photodetector is expected to contribute to high-performance and cost-effective optical/RF transducers.

### 4.1　はじめに

Optoelectric integrated circuits (OEIC's) are being investigated for use in fiber optic links, because they can reduce size and improve performance [1]. OEIC's made from GaAs-based materials are used in short-wavelength systems such as optical LAN and CATV networks. At present, fiber optic subcarrier transmission links are being investigated for use in personal communications. In such applications, a large number of radio base stations are

required for signal distribution to personal terminals [2]. Therefore, it is important to reduce the cost of radio base stations.

Monolithically integrated MSM photodetectors have been used in OEIC receivers due to their simple planar structures [3]. However, the responsivity of the MSM photodetector is quite low. As an alternative, HEMT photodetectors (HEMT-PD's) can be used. HEMT-PD's have structures and fabrication processes are compatible with those of GaAs MMIC's, therefore they are cost-effective. It should be added that HEMT's and MESFET's have been employed for high-speed optical pulse detection [4]. However, the fundamental properties of the HEMT-PD in fiber optic subcarrier transmission links have not been well characterized [5]. In this paper, the frequency response and noise performance of HEMT-PD's fabricated using the conventional MMIC process, are experimentally discussed. Such HEMT-PD's are expected to be used in fiber optic links, replacing pin-photodetectors. An optical MMIC receiver that employs the HEMT-PD and distributed amplifiers is also demonstrated.

### 4.2 光ファイバリンクによる実験

The experimental setup for electro-optic on-wafer measurement of the photodetectors is shown in Fig. 27. The frequency response of the photodetectors was measured with an HP8703A network analyzer. The noise performance was evaluated with a spectrum analyzer as a function of illuminated optical power, and a low noise pre-amplifier was used to reduce the analyzer noise. To evaluate the wide-band performance, a 0.83 $\mu$m-wavelength optical source and a $LiNbO_3$ external optical modulator (EOM) were used together as an optical transmitter, and the modulation depth of the EOM for subcarrier

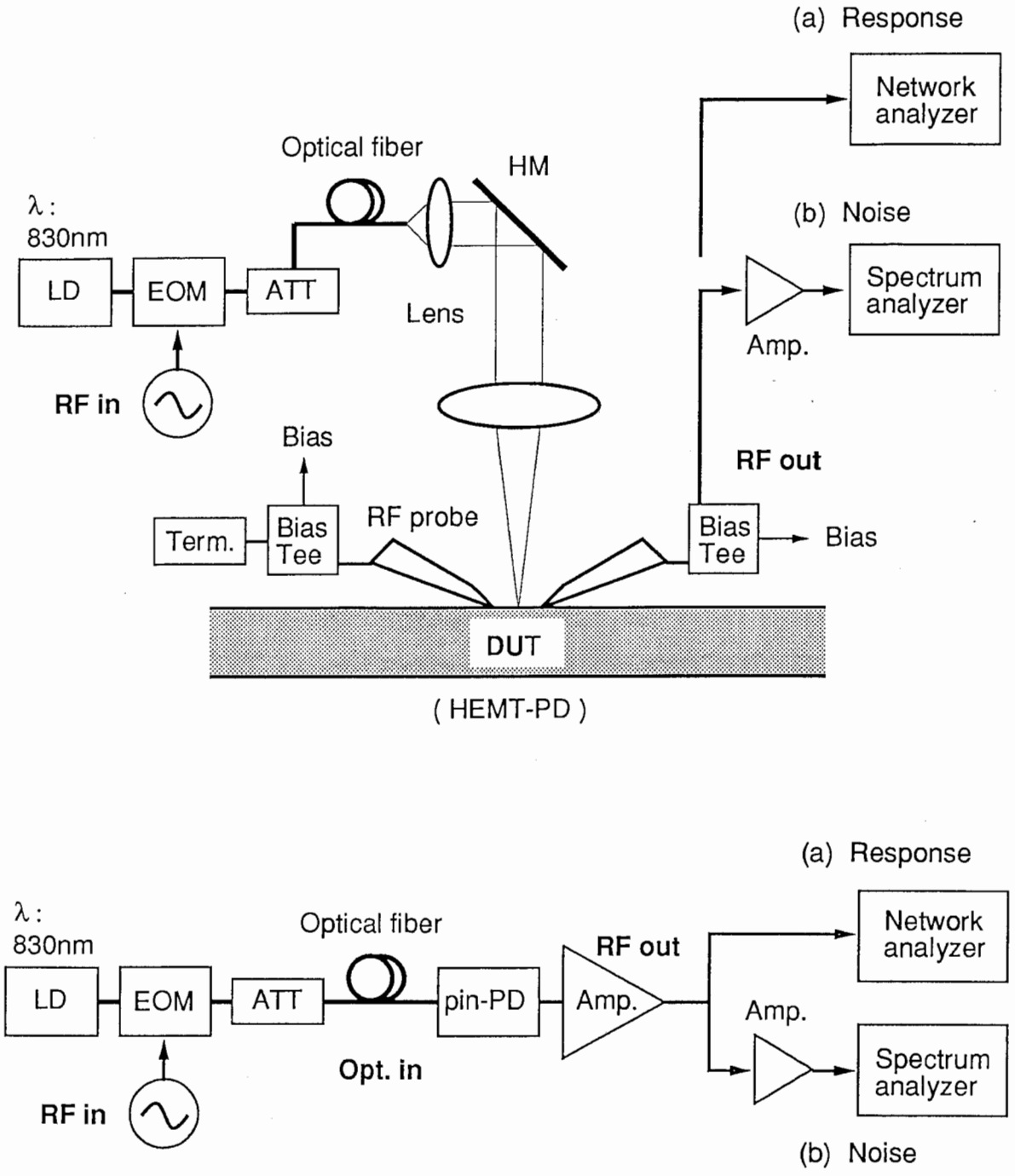


**Fig. 27** Experimental setup for electro-optic on-wafer measurement of the photodetectors. (a) Frequency response measurement and (b) noise measurement.

signals was 70 % at 1 GHz. Since the HEMT-PD's were fabricated on a GaAs wafer, an on-wafer microwave probe station was also employed to detect the subcarrier. The input optical beam was focused on a HEMT-PD through an optical fiber and beam collimation lens using a long working-distance microscope objective lens. The spot diameter and maximum illuminated optical power were 20 $\mu$m and 0.39 mW, respectively.

The AlGaAs/GaAs HEMT's with cut-off frequencies of up to 40 GHz have a gate length of 0.25 $\mu$m. In our experiment, the input port of the HEMT-PD was terminated with a 50 $\Omega$-load, and the drain voltage was set at 2 V. The optical carrier illuminated the active layer around the intrinsic gate region, between the source and drain electrodes. Therefore, the coupling efficiency was reduced due to the narrow length of the active layer. Although the coupling efficiency was less than 20 %, the measured drain current responsivity was approximately 1.9 A/W at zero gate bias, a value higher than that of the pin-PD. The HEMT-PD exhibited a much higher photocurrent gain due to the photoconductive and photovoltaic effects in the active layer [6].

### 4.3 周波数応答

The frequency response of HEMT-PD's with gate widths of 25 $\mu$m, 50 $\mu$m, 100 $\mu$m and 200 $\mu$m are shown in Fig. 28. That of a pin-photodiode (pin-PD module) with a 0.30 A/W responsivity and a 10 GHz bandwidth, is also measured for a performance comparison. Since the response of the EOM is substracted from the total link gain, the frequency response values show the intrinsic values of the photodetectors. The responses of the HEMT-PD's are slightly higher when the gate width is narrow. For example, the response of

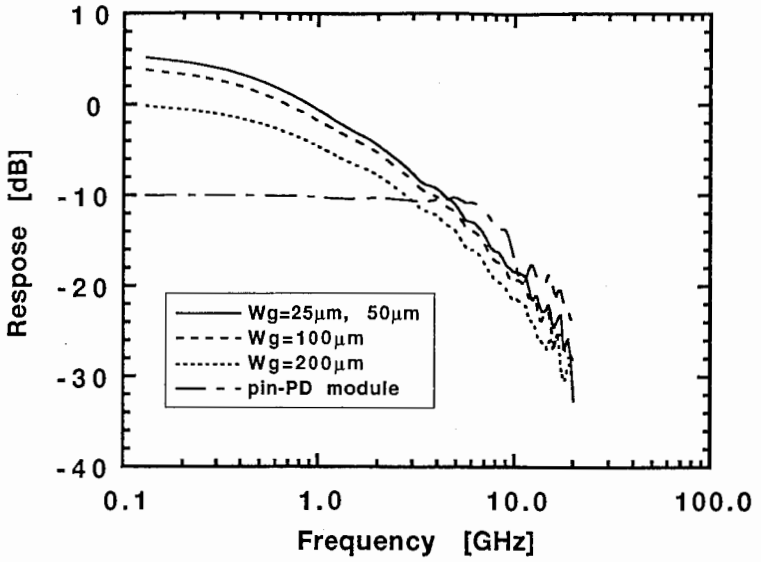


**Fig. 28** Frequency response of HEMT-PD's and pin-PD. A 0 dB response corresponds to a responsivity of 1 A/W ( $R_{DB} = 20 \log R_{MAG}$ ). The gate bias of each HEMT-PD is optimized for the SNR.

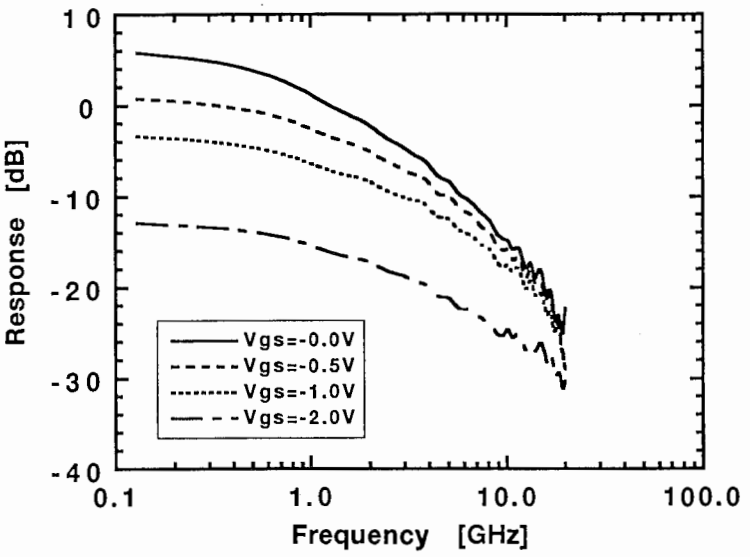


**Fig. 29** Gate bias dependence of the HEMT-PD response (Wg = 25 $\mu$m, Vds = 2 V).

the 25 $\mu$m-gate-width HEMT-PD is 10 dB greater than that of the pin-PD at a frequency of 1 GHz. At frequencies above 5 GHz, the responses of the HEMT-PD's become the same as that of the pin-PD. Then, up to 20 GHz, they drop rapidly with increasing subcarrier frequency, and range from 5 dB to $-25$ dB.

The gate bias dependence of the frequency response is shown in Fig. 29. The response of the HEMT-PD rapidly decreases with higher gate bias voltage at frequencies of up to 5 GHz. This show that the frequency response is dependent on the gate and drain voltages, and is not strongly dependent on the gate width. The response speed of the photoconductive current and the photovoltaic current, which are key factors in HEMT photodetection, are limited by the mean carrier lifetime [7], [8]. Therefore, the frequency of the 3 dB-bandwidth decreases to a value of approximately 0.8 GHz.

### 4.4 雑音特性

Figures 30(a) and (b) show the detected output power and signal-to-noise ratio (SNR), respectively, for a fiber optic subcarrier transmission link composed of the HEMT-PD and an optical transmitter, as a function of illuminated optical input power. The measured noise bandwidth, subcarrier frequency and input signal level are set at 1 MHz, 1 GHz and 0 dBm, respectively. Values for a pin-PD with an amplifier (pin-AMP), which is the conventional configuration of an optical receiver, are also shown. The amplifier has a gain of 20 dB and a noise figure of 5.9 dB. The signal level of the HEMT drops linearly, and a noise equivalent power (NEP) of $-71$ dBm/$\sqrt{Hz}$ is obtained. Although the signal level of the HEMT-PD is approximately 8 dB

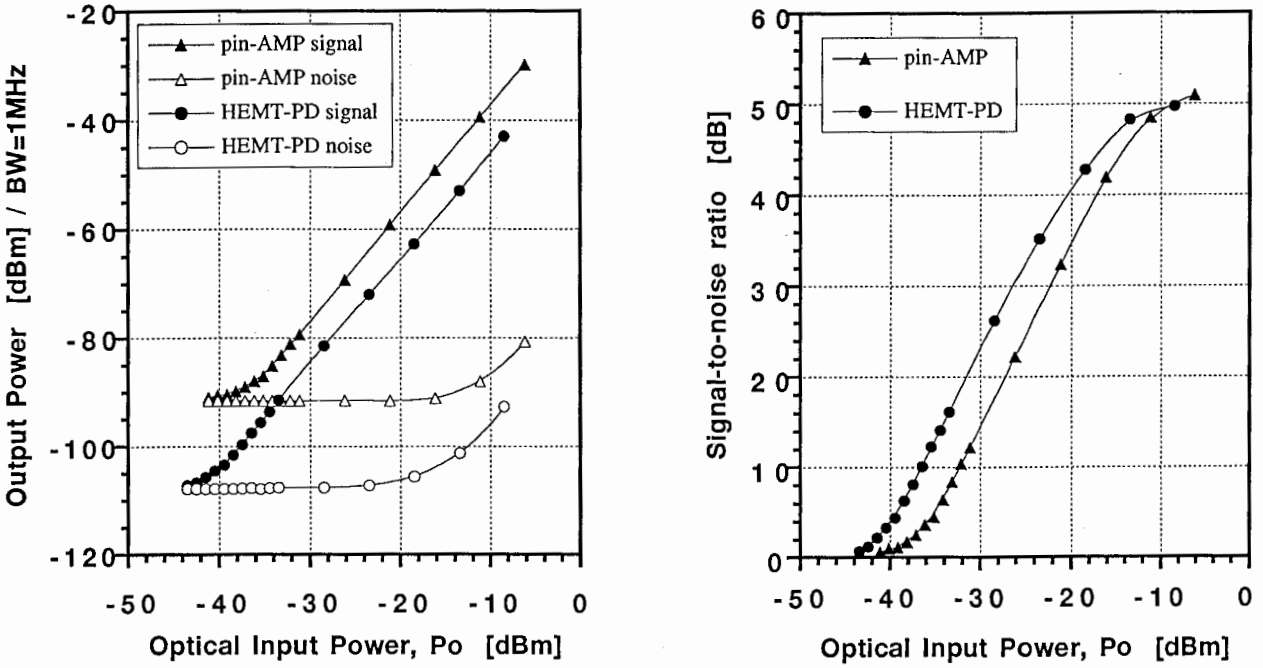


**Fig. 30(a)** Detected signal and noise level of the photodetectors as a function of optical input power. The measured bandwidth, sub-carrier frequency and power level are 1 MHz, 1 GHz and 0 dBm, respectively.

**Fig. 30(b)** Signal-to-noise ratio of the photodetectors.

lower than that of the pin-AMP, the noise level of the HEMT-PD is 16 dB lower. The SNR of the HEMT-PD whose gate width is 25 $\mu$m, is 8 dB lower than that of the pin-AMP as shown in Fig. 30(b) when the optical power is $-33$ dBm.

Figure 31 shows the SNR of the HEMT-PD's as a function of gate voltage. The SNR curves each show a ratio peak, and are strongly dependent on the gate width and gate voltage. These results show that the channel noise of the HEMT-PD's increases with increasing drain current, while the signal level of the HEMT-PD's rapidly decreases with decreasing drain current. Figure 32 shows the frequency dependence of the SNR. The measured HEMT-PD had a gate width of 25 $\mu$m. At frequencies of up to 5 GHz, the SNR of the HEMT-PD is larger than that of the pin-AMP.

### 4.5 光受信器への適用

To demonstrate the flexibility of circuit design using the HEMT-PD, we fabricated an optical receiver utilizing the conventional MMIC process. A microphotograph of the fabricated MMIC is shown in Fig. 33. The chip area is 1.55 mm $\times$ 1.7 mm. The MMIC is constructed with a cascade connection of HEMT-PD and microwave distributed amplifier. The amplifier block, which is constructed using 4-section HEMT's, exhibits a gain of 7.5 dB $\pm$ 0.5 dB, and the input/output return losses are better than 10 dB in the frequency range of 4 GHz to 30 GHz.

The measured and calculated characteristics of the MMIC are shown in Fig. 34. In the frequency range of 4 GHz to 20 GHz, the response of the fabricated MMIC is approximately 6 dB greater than that of the discrete

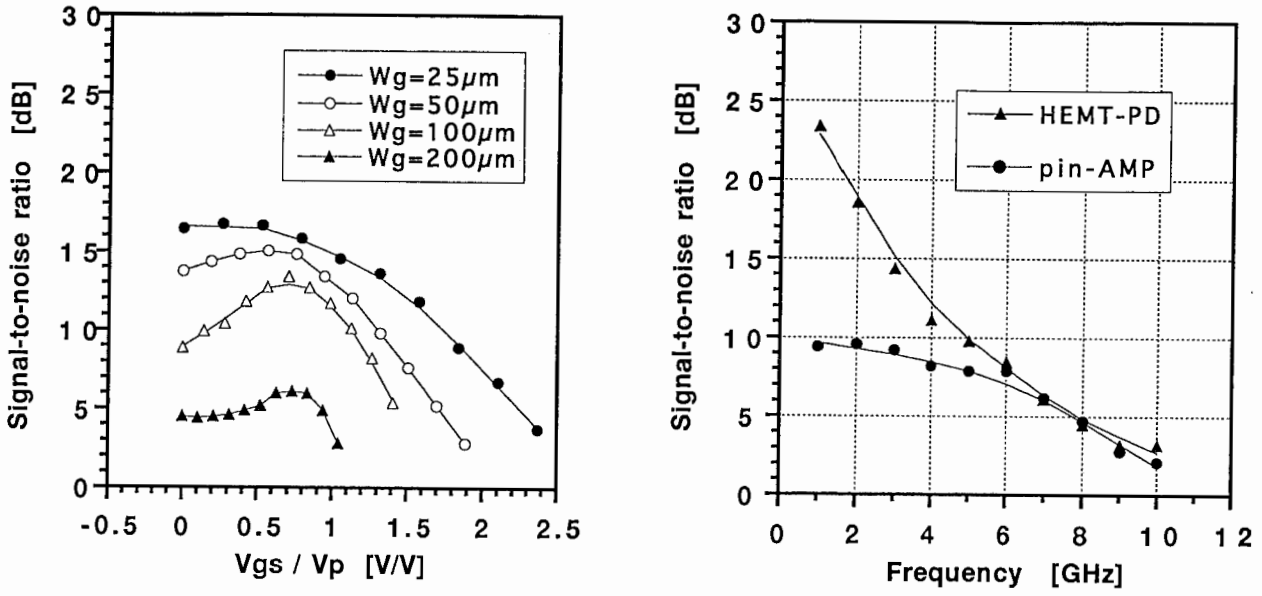


**Fig. 31** Signal-to-noise ratio of HEMT-PD's as a function of gate voltage. The illuminated optical power and subcarrier frequency are $-33$ dBm and 1 GHz, respectively.

**Fig. 32** Frequency characteristics of the signal-to-noise ratio. The illuminated optical power and spot diameter are $-31$ dBm and 10 $\mu$m, respectively.

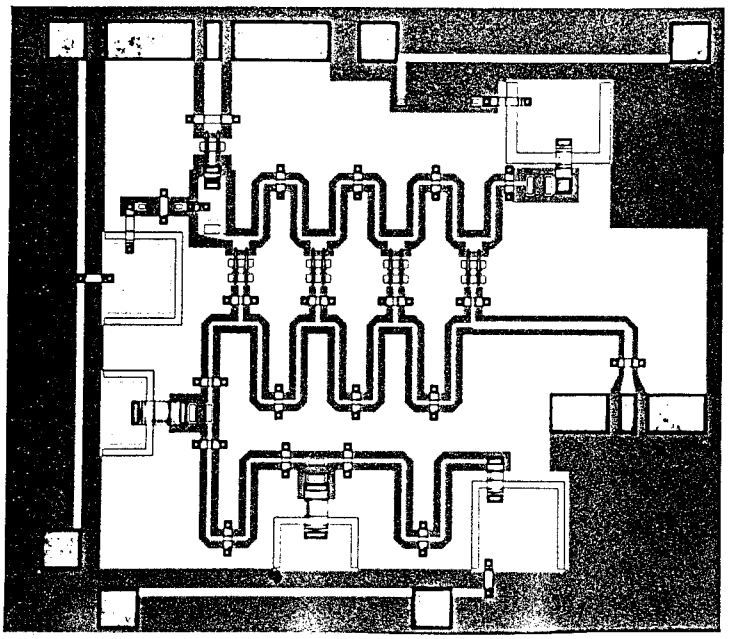

**Fig. 33** Microphotograph of a fabricated MMIC (1.55 mm × 1.7 mm).

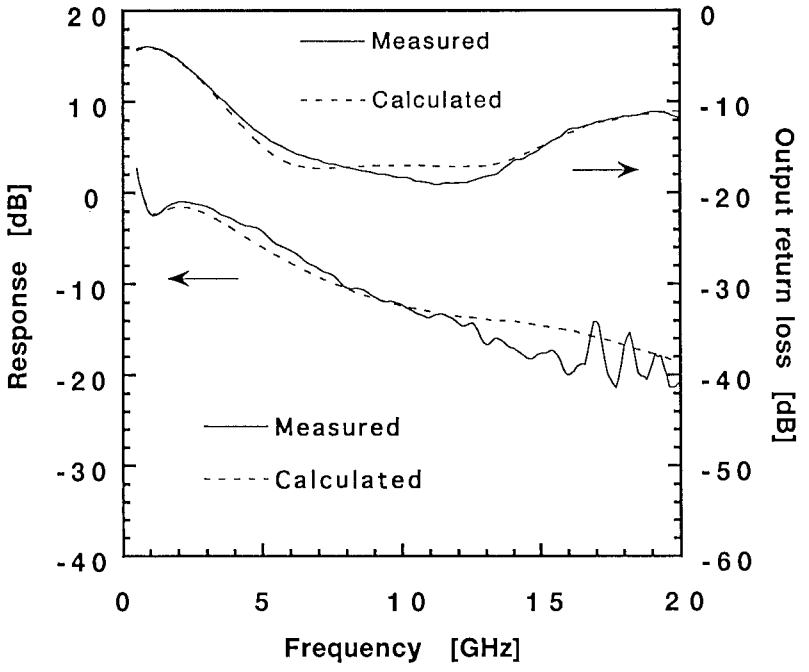


**Fig. 34** Characteristics of a fabricated MMIC.

HEMT-PD, as a result of the amplifier gain. The output return loss is better than 10 dB, while the return loss of the HEMT-PD is less than 2 dB.

## 4.6 まとめ

A monolithic integrable HEMT photodetector, whose device structure, fabrication process and bias conditions are compatible with those of GaAs MMIC's, has been introduced for use in fiber optic subcarrier transmission links. The photo response and noise performance of the HEMT-PD's were characterized, and an optical MMIC receiver was also demonstrated. Although the device structure of the HEMT-PD was optimized for microwave circuits, a photo response of 1.0 A/W and a signal-to-noise ratio of 49.8 dB were obtained at a frequency of 1 GHz. Therefore, MMIC HEMT's can be expected to contribute to low-noise and cost-effective optical/RF transducers.

## 参考文献


[1] O. Wada, T. Sakurai and T. Nakagami, "Recent Progress in Optoelectronic Integrated Circuits," *IEEE J. Quantum Electron.*, vol. **QE-20**, pp. 805-821, 1986.

[2] H. Ogawa, D. Polifko and S. Banba, "Millimeter-Wave Fiber Optics Systems for Personal Radio Communication," *IEEE Trans. Microwave Theory and Tech.*, vol. **MTT-40**, pp. 2285–2293, 1992.

[3] D. L. Rogers, "Integrated Optical Receivers Using MSM Detector," *IEEE J. Lightwave Tech.*, vol. **LT-12**, pp. 1635–1638, 1991.

[4] C. Baack, G. Elze and G. Walf, "GaAs M.E.S.F.E.T.: A High-Speed Optical Detector," *Electronics Lett.*, vol. **13**, pp. 193, 1977.

[5] A. Paolella, P. R. Herczfeld, A. Madjar and T. Higgings, "Optical Response of the GaAs MESFET at Microwave Frequencies and Applications," *IEEE MTT-S Int. Microwave Symp.*, pp. 487–490, 1991.

[6] A. A. Salles, "Optical Effect in HEMT," *Microwave and Optical Tech. Lett.*, vol. **3**, pp. 350–354, 1990.

[7] H. Beneking, "Gain and Bandwidth of Fast Near-Infrared Photodetectors: A Comparison of Diodes, Phototransistor, and Photoconductive Devices," *IEEE Trans. Electron Devices,* vol. **ED-29**, pp. 1420–1431, 1982.

[8] G. J. Papaionannou and J. R. Forrest, "On the Photoresponse of GaAs MESFET's: Backgating and Deep Traps Effect," *IEEE Trans. Electron Devices,* vol. **ED-33**, pp. 373–378, 1986.

# 5 光導波型デバイスの小型化（分岐型光導波路）

Symmetrical 3-branch optical waveguide structures, which can divide power equally at each branch, are proposed from calculations by the beam propagation method. The structure are constructed with a triangular shaped spacing area in the central branch to control the transmission coefficient between each branch and the main waveguide. The proposed 3-branch waveguides can be easily designed due to their simple configuration.

## 5.1 はじめに

Branching waveguides are important and essential components in optical integrated circuits. For instance, Y-branch waveguides that can divide power equally are employed as optical power dividers, switch arrays and interferometric modulators [1]-[3]. Symmetrical multibranch optical power dividers with equal power division, whose branch number is a power of 2, can be constructed using a cascade connection of Y-branch waveguides. However, they occupy a large circuit area. One of the most important problems in multibranch waveguides, with a branch number greater than two, is controlling the power ratio at each branch. Symmetrical 3-branch waveguides with equal power division for optical power dividers have been investigated [4]-[6]. However, these 3-branch waveguides are complicated and show large excess losses due to modifying the index distributions in the branches. In this letter, we propose a simple structure for a symmetrical 3-branch waveguide with equal

power division and also demonstrate the design curves.

## 5.2 多分岐光導波路の構成

A conventional 3-branch waveguide with a uniform index distribution, there is more power at the central branch, compared to the others. Therefore, the transmission coefficient between the central waveguide and the main waveguide is reduced by the spacing area in the central branch. The basic configurations of the proposed 3-branch waveguides are shown in Figures 35(a) and (b). In such cases, a two dimensional symmetrical slab geometry is assumed for simplicity. The proposed structures are different from the conventional structure in that the central branch has a triangular shaped spacing area. This area works to reduce the transmission coefficient between the main waveguide and the central branch. The waveguide width, branching angle and total length from the branching point to the end of the triangle are denoted by $T$, $\theta$ and $L$, respectively. When the spacing area is zero, the structure becomes a conventional 3-branch waveguide. When the spacing area is large the structure becomes a Y-branch-like structure, with a small transmission coefficient between the central waveguide and the main waveguide. Therefore, a symmetrical 3-branch waveguide with equal power division is obtained by controlling the spacing area which is formed area which is formed in the core region of the central branch. The structures are classified as follows:

(1) Conventional 3-branch for $L < T/2 \cdot \cot\theta$

(2) 3-branch with triangular shaped spacing for $T/2 \cdot \cot\theta < L < T \cdot \cot\theta$

(3) 3-coupled waveguide-like structure for $L > T \cdot \cot\theta$

The number of geometric parameters in the proposed structure is only one

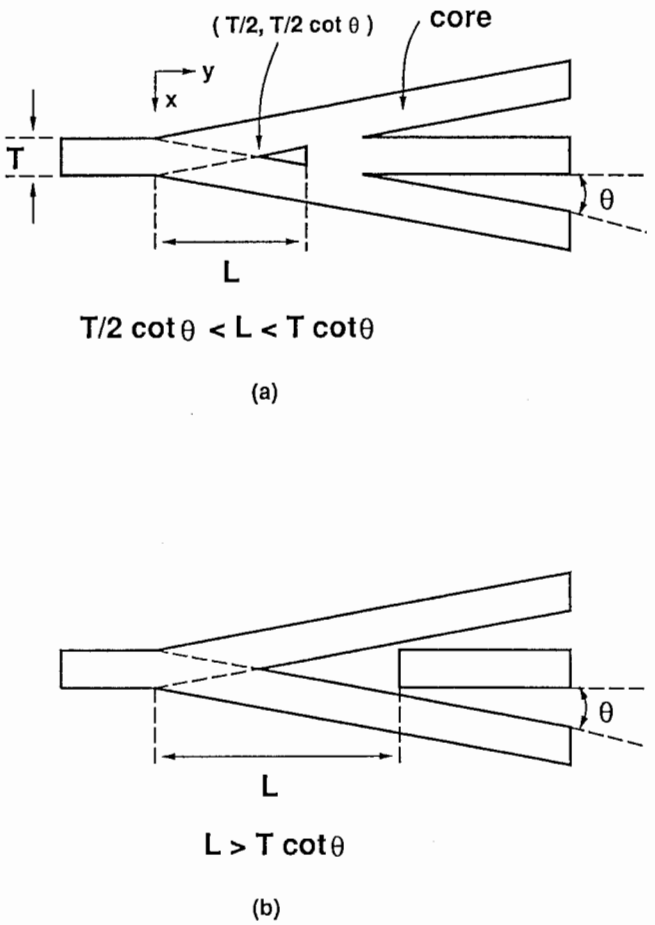


**Fig. 35** Proposed 3-branch waveguides. (a) 3-branch with triangular shaped spacing. (b) 3-coupled waveguide-like structure.

more than that of a conventional structure. Therefore, the proposed structures can easily be designed by the length $L$ and can be fabricated utilizing semiconductor device processing technologies such as dry etching or ion implantation.

## 5.3 ビーム伝搬法による設計

To demonstrate the field distribution of the proposed 3-branch structures, we employ the beam propagation method [7] (BPM) for numerical analysis. Each waveguide is assumed to operate in the $TE_0$ mode, and the operating wavelength and waveguide width are 1.0 $\mu$m and 6.6 $\mu$m, respectively. The index values of core, cladding and substrate are 1.502, 1.500 and 1.500, respectively. The effective index can be substituted in the dispersion equation in a homogeneous slab waveguide. The optical power ratio, $Pi$, is given by

$$Pi = \mid Ai/Ain \mid^2 \qquad (i = 1, 2, 3) \tag{11}$$

where the normalized field amplitude, $Ain$, in the main waveguide and $Ai$, in the $i-th$ branch are given by [4]. The optical power ratio of each branch as a function of length $L$ when the branching angle is 1.0 degree is shown in Fig. 36. In a conventional 3-branch waveguide (case 1), the power ratio of the central waveguide, P2, is greater than that of the other branches, P1 and P3. However, in the 3-branch waveguide with a triangular shaped spacing area (case 2), the power ratio of the center branch is decreased from 0.6 to 0.0 due to the increase in the length $L$, and the power ratio of the other branches is increased from 0.2 to 0.5. Power is equally divided at each branch when the length $L$ is 335 $\mu$m. The total power, Pt, of the various lengths $L$ slightly decreases compared with that of a conventional structure. The

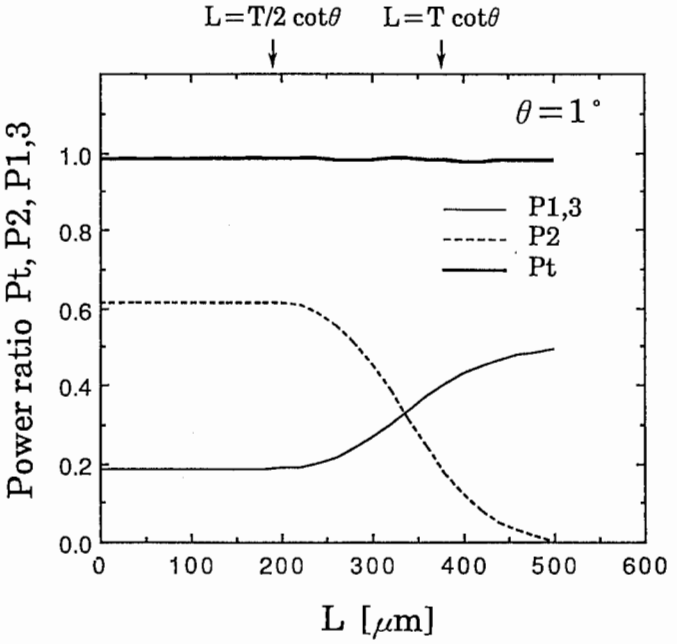


**Fig. 36** Power distribution in the proposed 3-branch structure as a function of spacing area length for $\theta = 1.0$ degree. (Propagation distance : 2000 $\mu$m, propagation step : 1 $\mu$m.)

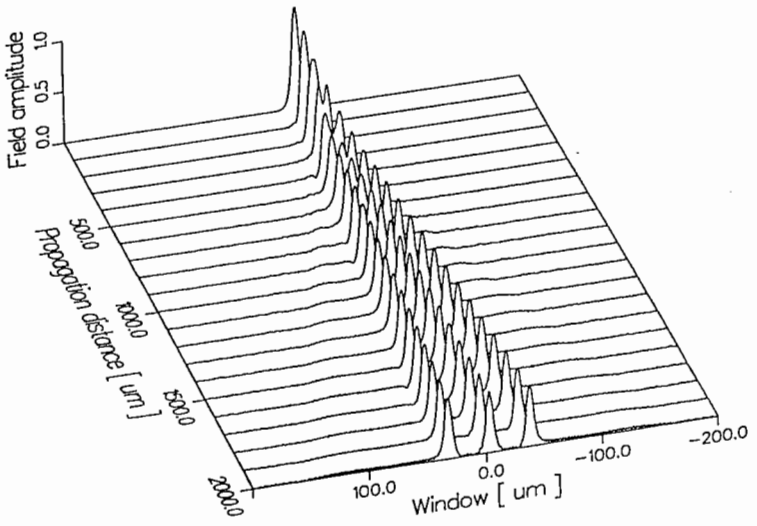


**Fig. 37** Field amplitude distribution for equal power division in a 3-branch with triangular spacing.

proposed 3-branch waveguides essentially have the antenna coupled structure reported in [8]. The antenna coupled Y-branch achieves a low junction loss when the branching angle is large. Therefore, the proposed structure achieves low branching losses in various cases. The field distribution in this condition is shown in Fig. 37. The propagation distance and propagation steps are 2000 $\mu$m and 1 $\mu$m, respectively. The power ratio of each branch as a function of the length $L$ when the branching angle is 0.5 degrees is shown in Fig. 38. In this condition, the design curve shows a power peak due to the resonance between the central branch and the outer branches. The radiation effect in the spacing area is also important, since the wavefront becomes circular. Equal power division is obtained when the structure becomes a 3-coupled waveguides-like structure (case 3). Consequently, equal power division is obtained between approximately 0.75 and 1.5 degrees with the 3-branch, triangular shaped spacing structure, and is obtained at other branching angles with a 3-coupled waveguide-like structure.

## 5.4 まとめ

A Simple structure has been proposed to divide power equally in the 3-branch waveguide. Equal power division was achieved by forming a triangular shaped spacing in the central branch. The proposed structures can be used for optical power dividers whose output port numbers are $2^N \times 3^M$. Furthermore, these structures can be applied to 4- or 5-branch waveguides by using a similar spacing area. Therefore, various optical power dividers and switches can be designed in a small circuit area.

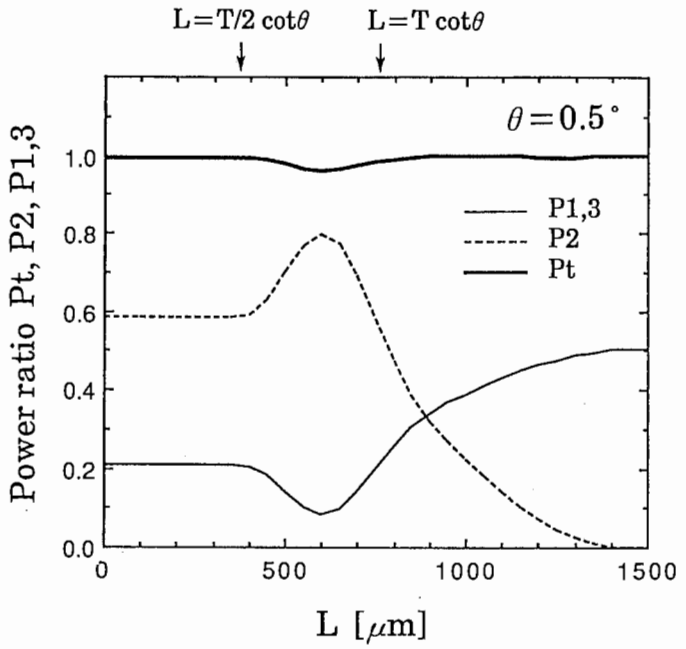


**Fig. 38** Power distribution in the proposed 3-branch structures as a function of spacing area length for $\theta = 0.5$ degrees. (Propagation distance : 4000 $\mu$m, propagation step : 1 $\mu$m.)

## 参考文献


[1] H. Sasaki and R. M. De La Rue, "Electro-optic Y-junction modulator/switch," *Electron. Lett.*, Vol. **12**, pp. 459–460, 1976.

[2] T. R. Ranganath and S. Wang, "Ti-diffused LiNbO3 branched-waveguide modulators : performance and design," *IEEE J. Quantum Electron.*, Vol. **QE-13**, pp. 290–295, 1977.

[3] M. Masuda and G. L. Yip, "An optical TE-TM mode splitter using a $LiNbO_3$ branching waveguide," *Appl. Phys. Lett.*, Vol. **37**, pp. 20–22, 1980.

[4] M. Belanger, G. L. Yip and M. Haruna, "Passive planar multibranch optical power divider : some design considerations," *Appl. Opt.*, Vol. **22**, pp. 2383–2389, 1983.

[5] W. Y. Hung, H. P. Chan and P. S. Chung, "Single-mode 1 × 3 integrated optical branching circuit design using phase-front accelerators," *Electron. Lett.*, Vol. **24**, pp. 1365–1366, 1988.

[6] G. L. Yip and M. A. Sekerka-Bajbus, "Design of symmetric and asymmetric passive 3-branch power dividers by beam propagation method," *Electron Lett.*, Vol. **24**, pp. 1584–1586, 1988.

[7] M. D. Feit and J. A. Fleck, Jr., "Computation of mode properties in optical fiber waveguides by a propagating beam method," *Appl. Opt.*, Vol. **19**, pp. 1154–1164, 1980.

[8] O. Hanaizumi, M. Miyagi and S. Kawakami, "Low radiation loss Y-junctions in planar dielectric optical waveguides," *Optics Communications*, Vol. **51**, pp. 236–238, 1984.

## 6　あとがき

報告者がＡＴＲ在籍中に担当した主な研究、多層化ＭＭＩＣおよび光マイクロ波集積回路について述べた。多層化ＭＭＩＣではその有効性を広く周知させ、光マイクロ波集積回路ではマイクロ波素子の光ファイバ通信への適用を示し、その有効性を確認した。さらに、これらの研究成果を踏まえて、新しい光マイクロ波（ミリ波）集積回路の概念を提唱した（第１３回光電波研究討論会資料参照）。


### 謝辞

本研究を進めるにあたって、直接ご指導頂いた小川博世主幹研究員（現在ＮＴＴ無線システム研究所）ならびに今井主任研究員に深謝いたします。また、本研究の遂行にあたり、討論を通じて有益なるご教示を頂いた葉原会長、古濱社長（現在ＣＲＬ）、猪股社長、赤池室長（現在東京理科大学）、小川英一室長ならびに無線通信第２研究室の皆様に感謝いたします。


## 研究発表リスト

### 参考文献


[1] Takao Hasegawa, Seiichi Banba, Hiroyo Ogawa and Hiroyuki Nakamoto, "Characteristics of Valley microstrip Lines for Use in Multilayer MMIC's," *IEEE Microwave and Guided Wave Letters,* Vol. **1**, No. 10, 1991.

[2] Seiichi Banba, Takao Hasegawa and Hiroyo Ogawa, "Multilayer MMIC Branch-Line Hybrid Using Thin Dielectric Layers," *IEEE Microwave and Guided Wave Letters,* Vol. **1**, No. 11, 1991.

[3] Takao Hasegawa, Seiichi Banba and Hiroyo Ogawa, "A Branchline Hybrid Using Valley Microstrip Lines," *IEEE Microwave and Guided Wave Letters,* Vol. **2**, No. 2, 1992.

[4] Seiichi Banba and Hiroyo Ogawa, "Novel Symmetrical Three-Branch Optical Waveguide with Equal Power Division," *IEEE Microwave and Guided Wave Letters,* Vol. **2**, No. 5, 1992.

[5] Seiichi Banba, Takao Hasegawa, Hiroyo Ogawa and Tsuneo Tokumitu, "Novel MMIC Transmission Lines Using Thin Dielectric Layers," *IEICE*

*Trans. Electron.,* Vol. **E75-C**, No. 6, 1992.

[6] Takao Hasegawa, Seiichi Banba, Hiroyo Ogawa and Tsuneo Tokumitsu, "Multi-Branch Power Dividers Using Multilayer MMIC Technology," *IEICE Trans. Electron.,* Vol. **E75-C**, No. 6, 1992.

[7] Hiroyo Ogawa, David Polifko and Seiichi Banba, "Millimeter-Wave Fiber Optics Systems for Personal Radio Communication," *IEEE Trans Microwave Theory and Techniques,* Vol. **MTT-40**, No. 12, 1992.

（2）学会発表 ２７件

[8] 小川博世、竹中　勉、長谷川隆生、馬場清一、上綱秀樹、「光ファイバリンクミリ波パーソナル通信システム」、電子情報通信学会秋季全国大会 １９９０年３月

[9] Hiroyo Ogawa, Takao Hasegawa, Seiichi Banba and Hiroyuki Nakamoto, "MMIC Transmission Lines For Multi-Layerd MMIC's," *1991 IEEE MTT-S Digest*

[10] 馬場清一、長谷川隆生、小川博世、中本博之、「多層化MMIC伝送線路」、電子情報通信学会春季全国大会 １９９１年３月

[11] 馬場清一、長谷川隆生、小川博世、「多層化MMIC伝送線路を用いた超小型ハイブリッド回路」、電子情報通信学会秋季全国大会 １９９１年９月

[12] 長谷川隆生、馬場清一、小川博世、「V溝MMIC伝送線路を用いたブランチラインハイブリッド」、電子情報通信学会秋季全国大会 １９９１年９月

[13] 小川博世、馬場清一、長谷川隆生、竹中　勉、上綱秀樹、「多層化MMICおよびミリ波伝送線路」、電気・情報関連学会連合大会 １９９１年９月

[14] 長谷川隆生、馬場清一、小川博世、「多層化MMICを用いた多分岐電力分配器」、電子情報通信学会技術研究報告会　マイクロ波研究会 １９９１年１０月

[15] 馬場清一、長谷川隆生、小川博世、「多層化MMICによる超小型ハイブリッド回路の構成と特性」、電子情報通信学会技術研究報告会　マイクロ波研究会 １９９１年１２月

[16] Hiroyo Ogawa, Hideki Kamitsuna, Seiichi Banba, Eiji Suematsu and Masami Akaike, "Millimeter-Wave Subcarrier Transmission Using Optoelectric Mixing and Optical Heterodyne Techniques," *1992 URSI International Symposium on Signals, Systems and Electronics.*

[17] 小川博世、馬場清一、上綱秀樹、竹中　勉、「光マイクロ波集積回路の構成法」、電子情報通信学会春季全国大会 １９９２年３月

[18] 上綱秀樹、馬場清一、小川博世、「HEMT MMIC の光・マイクロ波周波数混合特性とその応用に関する検討」、電子情報通信学会春季全国大会 １９９２年３月

[19] 馬場清一、上綱秀樹、小川博世、「HEMT 光応答特性の基礎検討」、電子情報通信学会春季全国大会 １９９２年３月

[20] 小川博世、デビィッド・ポリフコ、馬場清一、「ミリ波サブキャリア伝送用光ファイバリンクの検討」、電子情報通信学会技術研究報告会　マイクロ波研究会 １９９２年５月

[21] 馬場清一、上綱秀樹、小川博世、「マイクロ波・ミリ波デバイスによる光検出の検討」、電子情報通信学会技術研究報告会　マイクロ波研究会 １９９２年６月

[22] Hiroyo Ogawa, Seiichi Banba, Hideki Kamitsuna and David Polifko "Ka-Band FM Video Subcarrier Transmission Using Monolithic Integrated HEMT Photodetector," *Fourth Optoelectoronics Conference (OEC'92),* July 1992.

[23] 馬場清一、上綱秀樹、小川博世、「HEMT 光応答を用いた MMIC 光受信器」、電子情報通信学会秋季全国大会 １９９２年９月

[24] 末松英治、馬場清一、上綱秀樹、小川博世、「マイクロ波 HBT の光検波器への適用」、電子情報通信学会技術研究報告会　マイクロ波研究会 １９９２年９月

[25] 末松英治、馬場清一、上綱秀樹、小川博世、「マイクロ波 HBT 光検波器」、電子情報通信学会秋季全国大会 １９９２年９月

[26] 上綱秀樹、馬場清一、小川博世、「MMIC の光・マイクロ波周波数混合に関する一検討」、電子情報通信学会秋季全国大会 １９９２年９月

[27] Hiroyo Ogawa, Hideki Kamitsuna, Seiichi Banba and Eiji Suematsu, "Optical/Microwave Monolithic Integrated Circuits," *1992 Microwave Workshops and Exhibition -MWE'92-,* Sept., 1992.

[28] Seiichi Banba, Eiji Suematsu and Hiroyo Ogawa, "Fundamental Properties of HEMT Photodetector for Use in Fiber Optic Links," *23rd European Microwave Conference,* 1993.

[29] Hiroyo Ogawa, Seiichi Banba, Eiji Suematsu, Hideki Kamitsuna and David Polifko, "A Comparion of Noise Performance between a PIN Diode and MMIC HEMT and HBT Optical Receivers," *1993 IEEE MTT-S Digest*

[30] 上綱秀樹、馬場清一、小川博世、「MMIC プロセスを用いたモノリシックイメージ抑圧型光・マイクロ波周波数アップコンバータ」、電子情報通信学会春季全国大会 １９９３年３月

[31] 末松英治、馬場清一、上綱秀樹、小川博世、「MMIC HBT 光検出器の周波数特性」、電子情報通信学会春季全国大会 １９９３年３月

[32] 馬場清一、上綱秀樹、末松英治、小川博世、「HEMT 光検出器の雑音特性」、電子情報通信学会春季全国大会 １９９３年３月

[33] 馬場清一、小川博世、「多層化 MMIC による方向性結合器の構成と特性」、電子情報通信学会技術研究報告会　マイクロ波研究会 １９９３年１２月

[34] 馬場清一、小川博世、「多層化 MMIC による方向性結合器」、電子情報通信学会春季全国大会（投稿済み） １９９４年３月

（３） 特許出願　２件

[35] 「方向性結合器」、馬場 （外国出願手続き中）

[36] 「MMIC 付きアンテナ」、馬場、竹内

（４）その他　論文３件

[37] Seiichi Banba and Hiroyo Ogawa, "Small-Sized MMIC Amplifiers Using Thin Dielectric Layers," *IEEE Trans.Microwave Theory and Techniques* （投稿中）

[38] Seiichi Banba and Hiroyo Ogawa, "Multilayer MMIC Directional Couplers Using Thin Dielectric Layers," *IEEE Trans.Microwave Theory and Techniques* （投稿予定）

[39] Nobuaki Imai, Seiichi Banba, Eiji Suematsu and Hisashi Sawada, "Millimeter-wave Fiber optic Technologies for Subcarrier Transmission Systems," *24th European Microwave Conference,* 1994 （投稿中）